

An Atlas of Classical Pyrochlore Spin Liquids

Daniel Lozano-Gómez,^{1,2} Owen Benton,³ Michel J. P. Gingras,² and Han Yan (闫寒)^{4,*}

¹*Institut für Theoretische Physik and Würzburg-Dresden Cluster of Excellence ct.qmat,
Technische Universität Dresden, 01062 Dresden, Germany*

²*Department of Physics and Astronomy, University of Waterloo, Waterloo, Ontario N2L 3G1, Canada*

³*School of Physical and Chemical Sciences, Queen Mary University of London, London, E1 4NS, United Kingdom*

⁴*Institute for Solid State Physics, The University of Tokyo, Kashiwa, Chiba 277-8581, Japan*

(Dated: April 3, 2025)

Frustrated magnetism in the pyrochlore lattice magnet has proven to be a most fruitful setting for the experimental and theoretical search for spin liquids. Besides the canonical case of spin ice, recent works have identified a variety of new classical and quantum spin liquids engendered by the generic nearest-neighbor anisotropic spin Hamiltonian for that lattice. However, a general framework for the thorough and systematic classification and characterization of these exotic states of matter has been lacking, as has an *exhaustive* list of all possible spin liquids that this model can support and, perhaps most interesting, what is the corresponding structure of their emergent field theory description. In this work, we develop such a theoretical framework to identify the interaction parameters stabilizing different classical spin liquids and derive their corresponding effective generalized Gauss’s laws at low temperatures. Combining this with Monte Carlo simulations, we systematically identify all classical spin liquids for the general nearest-neighbor anisotropic spin Hamiltonian on the pyrochlore lattice. In doing so, we uncover new spin liquid models with exotic forms of generalized Gauss’s law and multipole conservation laws. Our approach allows us to compile an atlas of all spin liquids realized in the phase diagram, providing a global picture of their mutual connections in parameter space and transitions between them. Our work will inform future theoretical and experimental studies of classical and quantum spin liquids on the pyrochlore lattice and help rationalize the exotic properties of pyrochlore magnets.

I. INTRODUCTION

The exploration of quantum and classical spin liquids (CSLs) stable down to the lowest temperatures has been one of the most active pursuits in many-body physics over the past thirty years [1–8]. These phases, whose spins are disordered yet highly correlated, develop at low temperatures and are described by effective gauge theories emerging from the microscopic spin degrees of freedom (DOFs). For example, CSLs often realize the electrostatic sector of gauge theories [9–11]. When quantum fluctuations are introduced, these CSLs may become quantum spin liquids, which exhibit topological entanglement, fractionalized excitations, and, in gapped cases, topological order—some of the most fascinating phenomena in quantum matter. Classical spin liquids typically arise from finely tuned spin-spin interactions on specific lattice geometries, often featuring geometric frustration [12]. This frustration stabilizes highly degenerate classical ground states [2, 3] leading to collective paramagnetic behavior [13] and, in some cases, providing a potential route to quantum spin liquid phases [2, 5–7].

In particular, the pyrochlore lattice, a network of corner-sharing tetrahedra [2, 14–17], has provided a fruitful landscape for the search of spin liquids. The first and most canonical example is classical spin ice [18–21], experimentally realized in $\text{Ho}_2\text{Ti}_2\text{O}_7$ [18, 22–24] and $\text{Dy}_2\text{Ti}_2\text{O}_7$ [25–27]. At low temperatures, this classical

spin liquid realizes an effective Maxwell U(1) electrostatics theory on the parent (or premedial) diamond lattice [28], whose ground states are divergence-free “electric field” configurations, and elementary excitations are sources and sinks (i.e. “charges”) of that field [20]¹. In other materials [16, 17], in which quantum effects [30] are expected to be more important than in the $(\text{Ho,Dy})_2(\text{Ti,Sn,Ge})_2\text{O}_7$ classical spin ice compounds [31], a quantum counterpart of spin ice realizing full-fledged quantum electrodynamics, namely quantum spin ice [6, 32], has been under intense theoretical [33–43] and experimental investigations [44–53].

Zooming out to the entire landscape, a much wider spectrum of exotic classical spin liquids have been discovered upon considering the generic nearest-neighbor anisotropic bilinear spin model on the pyrochlore lattice. This family of models, parameterized by four symmetry-allowed anisotropic spin-spin couplings of exchange origin ($\{J_{zz}, J_{\pm}, J_{\pm\pm}, J_{z\pm}\}$ [54–58]), has been successful in characterizing the low-temperature physics of several pyrochlore compounds $\text{R}_2\text{M}_2\text{O}_7$ [15–17], where R is a trivalent rare earth ion and M is a non-magnetic tetravalent transition metal ion [14].

These classical spin liquids are characterized by emergent *generalized* Gauss’s laws [9, 10, 59–61]. Among

* hanyan@issp.u-tokyo.ac.jp

¹ Often, the dual language of magnetic field and magnetic monopoles is used in the literature [6, 29].

them, classical spin ice [19], the Heisenberg antiferromagnet (HAFM) spin liquid [62, 63] and the XXZ model [64] host one or several copies of emergent Gauss’s law [28]. Other cases, such as the so-called pinch-line spin liquid [65] and the rank-1–rank-2 spin liquid [66] are more exotic; these are *higher-rank* spin liquids, whose generalized Gauss’s laws are imposed on tensorial (rank-2) electric fields. Such more complex versions of electrodynamics, which are allowed on the lattice due to the lack of Lorentz or rotational symmetry, would describe new gapless quantum spin liquids, and are closely related to the field of fractonic states of matter [67–69]. The intrinsic multipole conservation and subsystem symmetries showcased by these higher-rank spin liquids are at the root of a rich physics, from immobile fractionalized excitations dubbed fractons [60, 61, 70] to quantum error-correction [71, 72].

Apart from spin ice, which occupies a three-dimensional parameter space at zero temperature [16, 39, 57, 58], the other classical pyrochlore spin liquids that have been theoretically discovered generally live on the phase boundary of two or more magnetically ordered phases [65, 66]². While the phase diagram of the possible long-range magnetic orders for the general Hamiltonian has been discussed in detail in the literature [15, 16, 57, 75] (for a recent in-depth analysis of the irrep fields, and the geometry and topology of the phases and phase boundaries, see the recent work by Chung [58]), a theoretical framework to identify systematically *all* CSLs on the pyrochlore lattice is still lacking. This raises a key question: do additional, previously overlooked spin liquids exist in the phase diagram? In short, an “atlas” of classical spin liquids, i.e., a map showing the exact regions in parameter space where CSLs are realized and what their respective dualities are, and how different CSLs transition into each other remains wanting.

In this work, we address these shortcomings by developing such a theoretical framework based on irreducible representations of the symmetries of a tetrahedron (tetrahedral point group, T_d) and the inter-tetrahedra constraints created by the spin Hamiltonian, which together enable a comprehensive study of various pyrochlore classical spin liquids. Specifically, we identify all the classical spin liquids stabilized down to the lowest temperatures for the generic nearest-neighbor Hamiltonian on the pyrochlore lattice. Our approach also provides a straightforward recipe for constructing the low-energy effective generalized Gauss’s law for the different CSLs. We have found in total nine classical spin liquids and derived their gauge theories including two cases not previously discussed in the literature and which realize a Maxwell and a rank-2 U(1) electrostatics, respectively. This allows

us to chart an atlas of classical pyrochlore spin liquids, presenting both the exact parameter space that defines different CSLs, identify their dualities and map the phase transitions between them.

Our approach transforms the theoretical search for pyrochlore CSLs from smart craftsmanship to a rigorously organized and systematic procedure. Our work is also highly experimentally relevant: as shown in several previous studies [15, 52, 56, 57, 76–81], it turns out that, rather interestingly, many pyrochlore compounds find themselves rather close to the phase boundaries of semiclassical long-range magnetic orders where such multiphase competition is essential for understanding their physics. Our work, charting out the CSLs that live on these phase boundaries, will be useful to understand the exotic physics at play in past and future experiments. In particular, we discuss the exciting opportunities to realize fracton physics in these frustrated magnetic systems. Our atlas also provides a road-map for the systematic hunt for pyrochlore quantum spin liquids, as it highlights the parameter spaces of most intense competition between the various spin-spin interactions and indicates the potential nature of the prospective quantum spin liquids descending from their classical limits.

The rest of the paper is organized as follows: in Sec. II, we review salient aspects of the generic nearest-neighbor anisotropic bilinear model on the pyrochlore lattice and briefly summarize the results that follow. In Sec. III, we present the irreducible representation analysis of the spin Hamiltonian and show how this can be used to derive the underlying gauge fields and emergent Gauss’s laws characterizing the various classical spin liquid phases of the model. Using this procedure, we identify in Sec. IV and V the regions in parameter space where both already known as well as, to the best of our knowledge, heretofore unidentified classical spin liquid phases are realized. In Sec. VI, we show how the spin liquid regions in the $\{J_{zz}, J_{\pm}, J_{\pm\pm}, J_{z\pm}\}$ phase diagram intersect each other. In particular, we show that all the classical spin liquids in the generic nearest-neighbor Hamiltonian can be reached by continuously tuning the interaction parameters without an intermediate symmetry-broken phase bisecting them. Then, in Sec. VII, we provide numerical evidence for the $T \rightarrow 0$ stability of these unexplored spin liquids identified in Sec. V. Finally, we conclude the paper in Sec. IX with a general overview of our results and perspective for future work.

II. THE MODEL AND SUMMARY OF MAIN RESULTS

A. The nearest-neighbor pyrochlore model

This section summarizes the pyrochlore anisotropic spin model, the location of CSLs in its ground-state phase diagram, and the corresponding emergent Gauss’s laws for readers seeking a quick overview of our paper. For

² The existence of spin liquids on so-called breathing pyrochlore lattices has also been explored [73, 74]

TABLE I. Table of all classical spin liquids (CSLs) for the pyrochlore spin system with nearest-neighbor anisotropic spin-spin interactions [Eq.(1)]. The third column gives the irreps that achieve minimal a_x couplings [i.e. “fluctuating irrep” in Eq. (13)]. The corresponding irreducible representation order parameters become the electric field constrained by generalized Gauss’s laws. The fourth column shows the corresponding $J_{\mu\nu}$ spin-spin interaction parameters in Eq. (1) that define the CSL while the fifth column shows the dimension of that parameter space (an overall scaling of all the parameters is not considered). The sixth column lists the corresponding generalized Gauss’s laws of the CSLs, whose derivation is discussed in detail in this work. The seventh column lists some of the relevant references for previously identified CSLs.

NON-KRAMERS CLASSICAL SPIN LIQUIDS						
	type and name of CSL	fluctuating irreps	$J_{\mu\nu}$ interaction parameters	phase dim.	Gauss’s laws	Refs.
1	Single R1U1 (Spin ice)	$\mathbb{T}_{1,i}$	$J_{zz} > 0$ $-J_{zz} < -6J_{\pm}$ and $2J_{\pm} \pm 4J_{\pm\pm}$	3D	$\nabla \cdot \mathbf{E}^{\text{ice}} = 0$	[18]
2	Double R1U1 (SL_{\perp})	$\mathbb{T}_{1,p}, \mathbb{T}_2$	$J_{\pm\pm} = 0, J_{\pm} < 0$ $2J_{\pm} < 3J_{zz}$ and $-J_{zz}$	1D	$\nabla \cdot \mathbf{E}^A = 0$ $\nabla \cdot \mathbf{E}^B = 0$	[64]
3	Triple R1U1 (pHAF)	$\mathbb{T}_{1,i}, \mathbb{T}_{1,p}, \mathbb{T}_2$	$J_{zz} > 0$ $J_{zz} : J_{\pm} : J_{\pm\pm} = 2 : -1 : 0$	1D	$\partial_i E_{ij}^{\text{pHAF}} = 0$	[64, 82]
4	R1U1-R2U1 (R_1 - $R_2^{\mathbb{T}_1}$)	$\mathbb{T}_{1,i}, \mathbf{E}, \mathbb{T}_{1,p}$	$J_{zz} > 0$ $J_{zz} : J_{\pm} : J_{\pm\pm} = 6 : 1 : -2$	1D	$\nabla \cdot \mathbf{E}^{\text{ice}} = 0$ $\partial_i E_{ij}^{\mathbb{T}_1+\mathbf{E}} = 0$	[66]
5	R1U1-R2U1 (R_1 - $R_2^{\mathbb{T}_2}$)	$\mathbb{T}_{1,i}, \mathbf{E}, \mathbb{T}_2$	$J_{zz} > 0$ $J_{zz} : J_{\pm} : J_{\pm\pm} = 6 : 1 : 2$	1D	$\nabla \cdot \mathbf{E}^{\text{ice}} = 0$ $\partial_i E_{ij}^{\mathbb{T}_2+\mathbf{E}} = 0$	[66]
KRAMERS CLASSICAL SPIN LIQUIDS						
6	SV-R2U1 (SV \equiv Scalar-vector)	$\mathbb{T}_{1,-}, \mathbf{E}, \mathbb{T}_2$	$J_{z\pm} > 0$, Eq. (51)	2D	$ \epsilon^{ijk} \partial_i E_{jk}^{\text{SV}} = 0$ $\partial_i E_{ij}^{\text{SV}} = 0$	
7	SV-R2U1* (Pinch-line spin liquid)	$\mathbb{T}_{1,-}, \mathbf{E}, \mathbb{T}_2$	$J_{z\pm} < 0$, Eq. (51)	2D	$ \epsilon^{ijk} \partial_i E_{jk}^{\text{SV}} = 0$ $\partial_i E_{ij}^{\text{SV}} = 0$	[65]
8	Triple R1U1 (HAFM)	$\mathbb{T}_{1,-}, \mathbf{E}, \mathbb{T}_2, \mathbf{A}_2$	$J_{zz} : J_{\pm} : J_{\pm\pm} : J_{z\pm}$ $= -2 : 1 : 2 : 2\sqrt{2}$	1D	$\partial_i E_{ij}^{\text{HAF}} = 0$	[82]
9	Triple R1U1 (HAFM*)	$\mathbb{T}_{1,-}, \mathbf{E}, \mathbb{T}_2, \mathbf{A}_2$	$J_{zz} : J_{\pm} : J_{\pm\pm} : J_{z\pm}$ $= -2 : 1 : 2 : -2\sqrt{2}$	1D	$\partial_i E_{ij}^{\text{HAF}} = 0$	

those interested in a deeper dive into the technicalities, the subsequent sections provide a comprehensive discussion of the construction of the field theory and the details of the classical Monte Carlo (CMC) simulations.

A prominent family of magnetic pyrochlore materials is the rare-earth pyrochlore oxides $R_2M_2O_7$ (see Fig. 1). In these materials, a strong crystal electric field (CEF) often produces a well-separated ground-state doublet, with an energy gap significantly larger than the interaction scale [16, 83, 84]³. In such a scenario, it is convenient

to describe these doublets as pseudospin-1/2 degrees of freedom (DOFs), S_i^α , and to model the ion-ion superexchange interactions as interactions between these pseudospins [16, 30, 33–35, 56, 76, 89–91].

The allowed form of nearest-neighbor interactions between pseudospin components can then be determined by symmetry. When doing this, one must remember that the transformation of the pseudospins under lattice symmetries and time-reversal depends on the symmetry of the wave functions making up the CEF doublet [16]. Through this analysis, three cases can be distinguished: ‘dipolar’ Kramers in which the pseudospin transforms like an ordinary spin-1/2; ‘dipolar-octupolar’ Kramers in which one component of the pseudospin transforms like a magnetic octupole; and the non-Kramers case where one of the z component of S_i transforms like a magnetic

³ The Tb-based pyrochlores [16, 33, 85] and, to a lesser extent, the Er-based ones [16, 86–88] are examples where this crystal-field energy gap is quite a bit smaller than in the other $R_2M_2O_7$ compounds, with the consequences of such not yet fully understood.

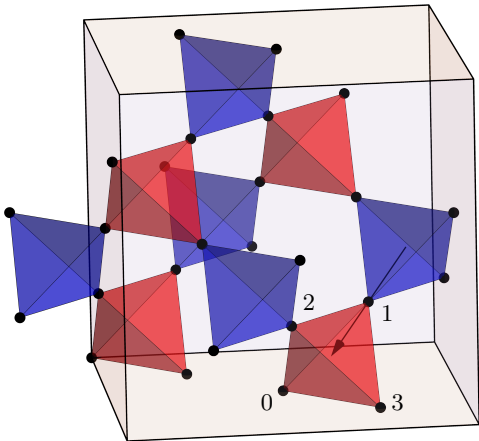


FIG. 1. Pyrochlore lattice where the spin degrees of freedom (DOFs) associated to the rare-earth R^{3+} ions in $R_2M_2O_7$ are located at the corners (black dots) of the tetrahedra. The M^{4+} ions reside on another regular pyrochlore lattice (not shown), that interpenetrates the one shown, and whose sites are located at the center of the hexagonal plaquettes defined by the R^{3+} ions [14]. We color the A and B tetrahedra in red and blue, respectively. Additionally, we illustrate the sublattice labels for the four sites of a single A tetrahedron along with the local z direction of the spin in sublattice 1 connecting the center of the adjacent tetrahedra sharing this lattice site.

dipole while the two other components transform like electric quadrupole moments (see Table 1 of Ref. [16]).

In the most general case, the nearest-neighbor Hamiltonian may be written as follows [56]

$$H_{\text{ex}} = \sum_{\langle ij \rangle} \left[J_{zz} S_i^z S_j^z - J_{\pm} (S_i^+ S_j^- + S_i^- S_j^+) + J_{\pm\pm} (\gamma_{ij} S_i^+ S_j^+ + \gamma_{ij}^* S_i^- S_j^-) - J_{z\pm} (\gamma_{ij}^* S_i^z S_j^+ + \gamma_{ij} S_i^z S_j^- + i \leftrightarrow j) \right], \quad (1)$$

where S_i^z is the component of the pseudospin directed along the local C_3 symmetry axis at each site (aligned with the local [111] direction connecting adjacent A and B tetrahedra), and S_i^{\pm} are raising and lowering operators defined relative to that axis. The γ_{ij} variables are bond-dependent phase factors which depend on the nature of the low energy CEF doublet [16, 34, 35, 56, 90]. For the dipolar Kramers [16, 56] and non-Kramers cases [16, 34, 35, 89], the γ_{ij} phase factors take on values

$$\gamma = \begin{pmatrix} 0 & 1 & c & c^* \\ 1 & 0 & c^* & c \\ c & c^* & 0 & 1 \\ c^* & c & 1 & 0 \end{pmatrix}, \quad (2)$$

where $c \equiv e^{2\pi i/3}$. For Kramers ions, all components of the pseudospin are odd under time reversal, while for non-Kramers ions the transverse S_i^{\pm} components are

time-reversal even. This has the important consequence that $J_{z\pm} = 0$ for non-Kramers ions [34, 35, 89]. Additionally, for the so-called dipolar-octupolar doublet Kramers systems [16, 39, 41, 90], such as the pyrochlores with Ce^{3+} , Sm^{3+} and Nd^{3+} rare-earth ions⁴, one has $\gamma_{ij} = 1$ on all nearest-neighbor bonds [90].

In the classical description of Eq. (1) we replace the S^{\pm} operators with $S^x \pm iS^y$ and treat $\mathbf{S} = (S^x, S^y, S^z)$ as a three-component vector of fixed length $S = 1$. Moreover, within a classical description, or within the context of materials with a larger spin value [92, 93], it is meaningful to consider a single-ion anisotropy term [92] whose simplest uniaxial form can be added to H_{ex} to give:

$$H = H_{\text{ex}} + H_{\text{si}}, \quad H_{\text{si}} = D \sum_i (S_i^z)^2. \quad (3)$$

In this work, we henceforth set $D = 0$ and focus on the H_{ex} terms only. Although we consider this simplified case, our field theory analysis could be straightforwardly generalized to the case with a non-zero H_{si} terms. We note that the results presented in this work focus on the classical Kramers and non-Kramers Hamiltonians, as the classical and quantum phase diagrams of the DO Hamiltonian [$\gamma_{ij} = 1$ in Eq. (1)] [90] have already been studied in detail in previous works [39, 41].

B. Main results

We comprehensively analyze the parameter space $\{J_{zz}, J_{\pm}, J_{\pm\pm}, J_{z\pm}\}$ for the classical dipolar spin system to map out *all* classical spin liquids in the phase diagram by combining analytical theory with CMC simulations. Analytically, we construct a long-wavelength field theory based on inter-tetrahedra constraints, unveiling various generalized Gauss's laws that characterize the degenerate ground states of different CSLs. This theoretical framework proves exact in the limit of a large number of spin components, \mathcal{N} . Through CMC simulations, we verify that the three-component classical version of the spin models (henceforth referred to as ' $\mathcal{N} = 3$ model' for short) remain disordered down to the lowest temperatures examined, and then further investigate the system's thermodynamic properties and spin-spin correlations. We note that the existence of an emergent Gauss's law from the large- \mathcal{N} field theory is a necessary but not sufficient condition for the manifestation of a CSL – there are cases in which the large- \mathcal{N} theory predicts a CSL but the $\mathcal{N} = 3$ model version eventually orders at low temperatures [94]. Such cases are usually associated with a thermal order-by-disorder selection [95, 96] that is typically induced by higher-order (fluctuation) terms in the

⁴ The classical $Dy_2(\text{Ti,Sn,Ge})_2O_7$ spin ices [31] with magnetic Dy^{3+} are also dipolar-octupolar materials [16, 90], albeit with rather small J_{\pm} , $J_{\pm\pm}$ and $J_{z\pm}$ transverse couplings in Eq. (1) [30].

free energy that are not included in the large- \mathcal{N} analysis [66].

We have identified a total of *nine* classical spin liquids (CSLs). The parameter spaces that define them and their corresponding emergent Gauss's laws are summarized in Table I. The generalized Gauss's laws include the conventional Maxwell Gauss's law, i.e., a charge as the divergence of a vector field, as well as more exotic forms such as coexisting two or three copies of Maxwell Gauss's law, charges defined by rank-2 matrix electric field as well as a mixture of them. In that table, we use a naming convention for the spin liquids based on the structure of the emergent gauge fields describing the low-temperature physics (R1 \equiv rank-1 or R2 \equiv rank-2), the gauge structure constraining the field (this being U1 \equiv U(1) for all the CSLs described in the present work), and then provide in parentheses the name these CSLs were given (if there was any) when first identified [18, 64–66, 82]. For example, for the spin ice CSL, the low-energy theory is described by a single rank-1 (R1) field with a U(1) (U1) structure characterized by the emergent Gauss's law acting on a rank-1 field. In our notation, this then reads as R1U1 (spin ice) spin liquid.

The four-dimensional phase diagram can be qualitatively divided into two regions based on the value of $J_{z\pm}$: one where $J_{z\pm} = 0$ (appropriate to non-Kramers materials), illustrated in Fig. 2, and another where $J_{z\pm} \neq 0$, illustrated in Fig. 3. The different CSLs are found within these distinct phase diagrams; the CSLs labeled 1 to 5 live in the $J_{z\pm} = 0$ phase diagram while the CSLs 6 to 9 live in the phase diagram of $J_{z\pm} \neq 0$. Except for spin ice (CSL 1), all other CSLs reside on the phase boundaries of magnetic orders. However, not all phase boundaries separating classical pseudospin long-range orders host CSLs.

Of the nine CSLs identified, several, such as spin ice and the Heisenberg antiferromagnetic (HAFM) model, have been individually explored in prior research. However, this study is the first to make a comprehensive study of their effective field theory, phase diagram, and transitions among them. Notably, the CSLs 6 and 9 have not been identified in previous literature, and we discuss below the properties of these two CSLs in some detail.

III. IRREDUCIBLE REPRESENTATIONS AND INTER-TETRAHEDRA CONSTRAINTS

A. Diagonalization of the single tetrahedron Hamiltonian

Every nearest-neighbor bond in the pyrochlore lattice belongs uniquely to one tetrahedron (A or B in Fig 1). The nearest-neighbor Hamiltonian H in Eq. (3) can therefore be expressed as a sum of terms over individual tetrahedra [57] which include a spin-spin exchange interaction term, $H_{\text{ex}}(t)$ and, for generality's sake, a single-

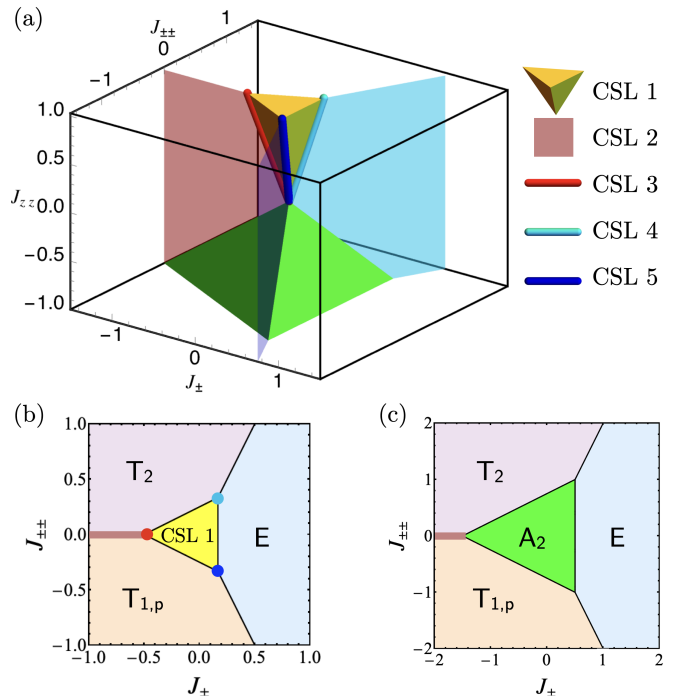


FIG. 2. (a) Phase diagram of classical spin liquids (CSLs) for the non-Kramers Hamiltonian [Sec. IV]. There are five CSLs in the phase diagram. CSL 1 (spin ice) occupies a 3D volume, CSL 2 occupies a surface, and the other three CSLs reside on different phase boundary lines. (b) Cross-section of the phase diagram at $J_{zz} = 1$, showing all five CSLs. The irreducible representations of the magnetic ordered phases are also indicated. (c) Cross-section at $J_{zz} = -1$. Only CSL 2 lives in this part of the phase diagram.

ion term, $H_{\text{si}}(t)$. We thus write H as

$$H = \sum_t H_t, \quad H_t = H_{\text{ex}}(t) + \frac{1}{2} H_{\text{si}}(t), \quad (4)$$

where $H_{\text{ex}}(t)$ and $H_{\text{si}}(t)$ are the exchange and single-ion Hamiltonians acting on a single tetrahedron, t . Here, the factor of 1/2 arises to avoid double-counting of the single ion term, since sites are shared by two tetrahedra.

The single-tetrahedron Hamiltonian H_t can then be re-expressed as a sum of quadratic terms:

$$H_t = \frac{1}{2} \left[a_{A_2} m_{A_2}^2 + a_E m_E^2 + a_{T_2} m_{T_2}^2 + (a_{T_{1,i}} m_{T_{1,i}}^2 + a_{T_{1,p}} m_{T_{1,p}}^2 + a_{T_{1,ip}} m_{T_{1,ip}} \cdot m_{T_{1,p}}) \right], \quad (5)$$

where each $m_{\mathcal{X}}$ is a local order parameter for different kinds of magnetic configuration corresponding to a particular irreducible representation (irrep) of T_d , the symmetry group of a tetrahedron, see Fig. 4.

We use the $m_{\mathcal{X}}$ notation to represent both the vector $m_{\mathcal{X}}$ irreps and scalar m irreps for simplicity of notation. Each $m_{\mathcal{X}}$ is defined by a specific linear combination of the spin components, which are given in Table II.

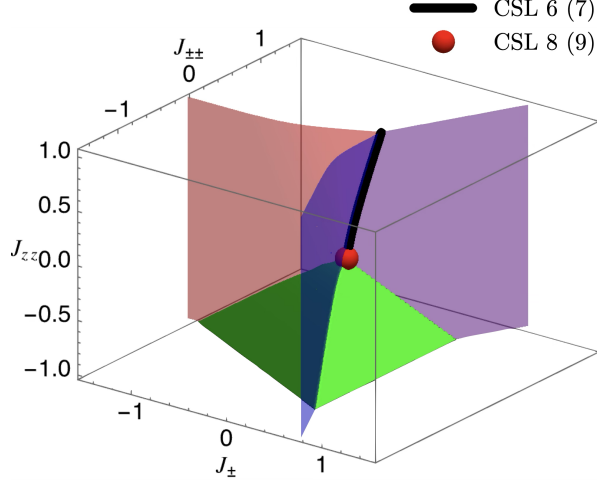


FIG. 3. Phase diagram of classical spin liquids (CSLs) for the Kramers Hamiltonian [Sec. V]. CSL 6 and 8 are realized in this phase diagram (here, $J_{z\pm}$ was taken to be 0.1). The CSL 6 is the scalar-vector rank-2 U(1) spin liquid, and lives on the phase boundary marked by a black line. CSL 8 is the Heisenberg antiferromagnet, corresponding to the red dot. By flipping the sign of the $J_{z\pm}$ coupling, i.e. $J_{z\pm} = -0.1$, the shape of the phase diagram remains invariant due to the duality in Eq. (60). Upon this $J_{z\pm} \rightarrow -J_{z\pm}$, CSL 6 becomes CSL 7 and CSL 8 becomes CSL 9.

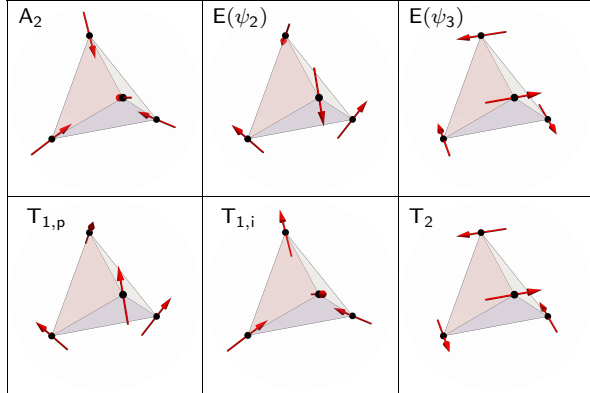


FIG. 4. Spin configuration of the irreducible representation configurations.

The labels A_2, E, T_1, T_2 correspond to different irreps of the point group of a tetrahedron according to which the different fields transform. The coefficients a_χ are linear combinations of the exchange interaction parameters $\{J_{zz}, J_\pm, J_{\pm\pm}, J_{z\pm}\}$ and the single-ion anisotropy D , as listed in Table III.

The coupling between $\mathbf{m}_{T_{1,i}}$ and $\mathbf{m}_{T_{1,p}}$, which both transforms according to T_1 , can be removed by a parameter-dependent redefinition of the fields. Specifically, we define:

$$\mathbf{m}_{T_{1,-}} = \cos\phi \mathbf{m}_{T_{1,i}} + \sin\phi \mathbf{m}_{T_{1,p}}, \quad (6)$$

$$\mathbf{m}_{T_{1,+}} = -\sin\phi \mathbf{m}_{T_{1,i}} + \cos\phi \mathbf{m}_{T_{1,p}}, \quad (7)$$

where

$$\mathbf{v}_- = \begin{pmatrix} v_{i-} \\ v_{p-} \end{pmatrix} \equiv \begin{pmatrix} \cos\phi \\ \sin\phi \end{pmatrix}, \quad (8)$$

$$\mathbf{v}_+ = \begin{pmatrix} v_{i+} \\ v_{p+} \end{pmatrix} \equiv \begin{pmatrix} -\sin\phi \\ \cos\phi \end{pmatrix}, \quad (9)$$

are the normalized eigenvectors of the 2×2 matrix

$$\begin{pmatrix} a_{T_{1,i}} & \frac{1}{2}a_{T_{1,ip}} \\ \frac{1}{2}a_{T_{1,ip}} & a_{T_{1,p}} \end{pmatrix},$$

with eigenvalues

$$a_{T_{1,-}} = \frac{1}{2} \left(a_{T_{1,i}} + a_{T_{1,p}} - \sqrt{(a_{T_{1,i}} - a_{T_{1,p}})^2 + a_{T_{1,ip}}^2} \right), \quad (10)$$

$$a_{T_{1,+}} = \frac{1}{2} \left(a_{T_{1,i}} + a_{T_{1,p}} + \sqrt{(a_{T_{1,i}} - a_{T_{1,p}})^2 + a_{T_{1,ip}}^2} \right), \quad (11)$$

respectively. Here, ϕ corresponds to the mixing angle between $\mathbf{m}_{T_{1,p}}$ and $\mathbf{m}_{T_{1,i}}$ due to non-zero $J_{z\pm}$,

$$\phi = \frac{1}{2} \arctan \left(\frac{a_{T_{1,ip}}}{a_{T_{1,i}} - a_{T_{1,p}}} \right). \quad (12)$$

With this redefinition of the T_1 fields, the diagonalized Hamiltonian for a single tetrahedron becomes:

$$H_t = \frac{1}{2} \left[a_{A_2} m_{A_2}^2 + a_E m_E^2 + a_{T_2} m_{T_2}^2 + a_{T_{1,-}} m_{T_{1,-}}^2 + a_{T_{1,+}} m_{T_{1,+}}^2 \right], \quad (13)$$

the sum of the squares of the \mathbf{m}_χ fields is constrained as a result of the spin normalization:

$$m_{A_2}^2 + m_E^2 + m_{T_2}^2 + m_{T_{1,-}}^2 + m_{T_{1,+}}^2 = 16S^2 \quad (14)$$

where $S \equiv |\mathbf{S}|$ is the spin length.

One begins by identifying which term in Eq. (13) has the lowest coefficient a_χ 's and use it as a baseline measure by subtracting it from all the other a_χ 's coefficients. Actually, there can be one or more a_χ being *simultaneously* minimal while also satisfying the spin normalization constrained in Eq. (14). Defining the minimal irrep coefficient as

$$\mathcal{E}_0 \equiv \min(a_{A_2}, a_E, a_{T_2}, a_{T_{1,-}}, a_{T_{1,+}}), \quad (15)$$

we then add and subtract $16\mathcal{E}_0 S^2$ from Eq. (13) and use Eq. (14) to obtain:

$$H_t = \frac{1}{2} \left[(a_{A_2} - \mathcal{E}_0) m_{A_2}^2 + (a_E - \mathcal{E}_0) m_E^2 + (a_{T_2} - \mathcal{E}_0) m_{T_2}^2 + (a_{T_{1,-}} - \mathcal{E}_0) m_{T_{1,-}}^2 + (a_{T_{1,+}} - \mathcal{E}_0) m_{T_{1,+}}^2 + 16S^2 \mathcal{E}_0 \right]. \quad (16)$$

TABLE II. Local order parameters \mathbf{m}_χ as irreducible representation (irrep) of T_d , the point group symmetry of a tetrahedron. The first column is the corresponding symmetry operation. The second column gives the corresponding magnetic phases. The third column lists the order parameter defined in terms of spins. Here the subscripts i and p refer to the ice and planar T_1 ferromagnetic single tetrahedron configurations, respectively.

Symmetry	Phase	Order parameter
$A_{2g} (\Gamma_3)$	all-in/all-out	$m_{A_2} = S_1^z + S_2^z + S_3^z + S_4^z$
$E_g (\Gamma_5)$	ψ phase	$\mathbf{m}_E = \begin{pmatrix} S_1^x + S_2^x + S_3^x + S_4^x \\ S_1^y + S_2^y + S_3^y + S_4^y \end{pmatrix}$
$T_{2g} (\Gamma_7)$	Palmer-Chalker	$\mathbf{m}_{T_2} = \begin{pmatrix} S_1^y + S_2^y - S_3^y - S_4^y \\ \left(-\frac{\sqrt{3}}{2}S_1^x - \frac{1}{2}S_1^y\right) - \left(-\frac{\sqrt{3}}{2}S_2^x - \frac{1}{2}S_2^y\right) + \left(-\frac{\sqrt{3}}{2}S_3^x - \frac{1}{2}S_3^y\right) - \left(-\frac{\sqrt{3}}{2}S_4^x - \frac{1}{2}S_4^y\right) \\ \left(\frac{\sqrt{3}}{2}S_1^x - \frac{1}{2}S_1^y\right) - \left(\frac{\sqrt{3}}{2}S_2^x - \frac{1}{2}S_2^y\right) - \left(\frac{\sqrt{3}}{2}S_3^x - \frac{1}{2}S_3^y\right) + \left(\frac{\sqrt{3}}{2}S_4^x - \frac{1}{2}S_4^y\right) \end{pmatrix}$
$T_{1g} (\Gamma_9)$	spin ice	$\mathbf{m}_{T_{1,i}} = \begin{pmatrix} S_1^z + S_2^z - S_3^z - S_4^z \\ S_1^z - S_2^z + S_3^z - S_4^z \\ S_1^z - S_2^z - S_3^z + S_4^z \end{pmatrix}$
$T'_{1g} (\Gamma_9)$	splayed ferromagnet	$\mathbf{m}_{T_{1,p}} = \begin{pmatrix} S_1^x + S_2^x - S_3^x - S_4^x \\ \left(-\frac{1}{2}S_1^x + \frac{\sqrt{3}}{2}S_1^y\right) - \left(-\frac{1}{2}S_2^x + \frac{\sqrt{3}}{2}S_2^y\right) + \left(-\frac{1}{2}S_3^x + \frac{\sqrt{3}}{2}S_3^y\right) - \left(-\frac{1}{2}S_4^x + \frac{\sqrt{3}}{2}S_4^y\right) \\ -\frac{1}{2}S_1^x - \frac{\sqrt{3}}{2}S_1^y - \left(-\frac{1}{2}S_2^x - \frac{\sqrt{3}}{2}S_2^y\right) - \left(-\frac{1}{2}S_3^x - \frac{\sqrt{3}}{2}S_3^y\right) + \left(-\frac{1}{2}S_4^x - \frac{\sqrt{3}}{2}S_4^y\right) \end{pmatrix}$

TABLE III. Coefficients of the irreducible representations in Eq. (5) in terms of exchange parameters and single-ion anisotropy in Eq. (1).

Coefficient	Definition in terms of exchange parameters $\{J_{zz}, J_\pm, J_{\pm\pm}, J_{z\pm}, D\}$
a_{A_2}	$3J_{zz} + D$
a_E	$-6J_\pm$
a_{T_2}	$2J_\pm - 4J_{\pm\pm}$
$a_{T_{1,i}}$	$-J_{zz} + D$
$a_{T_{1,p}}$	$2J_\pm + 4J_{\pm\pm}$
$a_{T_{1,ip}}$	$-8J_{z\pm}$

Each multiplicative prefactor in Eq. (16) is either vanishing (when $a_\chi = \mathcal{E}_0$) or strictly positive. From that equation, we can directly read off the ground state constraints for any $\{J_{zz}, J_\pm, J_{\pm\pm}, J_{z\pm}, D\}$ parameter set:

$$\sum_{\chi} \mathbf{m}_\chi^2 = 16S^2 \forall \chi \text{ such that } a_\chi = \mathcal{E}_0; \quad (17)$$

$$\mathbf{m}_\chi = 0 \forall \chi \text{ such that } a_\chi > \mathcal{E}_0. \quad (18)$$

These constraints are applied to every tetrahedra t . In

the zero temperature ($T \rightarrow 0$) limit, the components of the X irreps are free to fluctuate and these therefore correspond to the fluctuating DOFs that remain at low T . On the other hand, the Y irreps become ultimately frozen and introduce constraints on the ground state spin configurations. If there are enough DOFs among the \mathbf{m}_χ fields, then the first condition [Eq. (17)] does not sufficiently pin down the value of each \mathbf{m}_χ to induce magnetic order. In such a case, we may treat \mathbf{m}_χ 's as almost freely fluctuating at the level of a single tetrahedron. As we discuss in Subsection III B below, Eq. (18) will be used in conjunction with the inter-tetrahedra constraints defined by Eq. (17) to derive the Gauss's laws that emerge in the system and control its ground state properties.

B. Inter-tetrahedra constraints and coarse-graining

Equation (18) establishes a generalized set of constraints which, in a ground state, must be fulfilled on every tetrahedra of the lattice. The problem of fulfilling these constraints is rendered nontrivial by the fact that these are not independent: neighboring tetrahedra share a spin. So the ground state condition on one tetrahedron, say of type A , must also be respected by its four neighboring tetrahedra, say of type B .

To understand the consequences of this, it is useful to divide the pyrochlore tetrahedra into two sets of tetrahedra, labeled A and B , such that the neighbors of an A

tetrahedron are all B tetrahedra and vice versa, see Fig. 1. The centers of the A and B tetrahedra each form a pair of face-centered cubic (FCC) lattices, the two types together forming a bipartite diamond lattice.

One can then place the A tetrahedra into ground state configurations independently since they do not overlap with each other. Specifying a ground state configuration on the A tetrahedra amounts to setting the values of all the $\mathbf{m}_Y = 0$ according to the energetic constraint given by Eq. (18) (i.e. those for which $a_Y > \mathcal{E}_0$), while freely choosing a certain combination of the other \mathbf{m}_X fields, up to spin normalization constraints. Since every spin is included in exactly one A tetrahedron, and since the map between the \mathbf{m} fields and the spins is invertible, this construction completely determines the allowed spin configurations in the A tetrahedra when these are taken independently.

However, the \mathbf{m}_X 's on A tetrahedra have an additional constraint. In order to be a ground state, the spin configuration, or equivalently the \mathbf{m} fields, must also satisfy the constraints on the B tetrahedra. Or, in other words, the constraint requirements on a B tetrahedron constrains the \mathbf{m}_X fields on the four A tetrahedra surrounding it⁵. Using the relationship between the spins in the B tetrahedron and the \mathbf{m}_X fields on the A tetrahedra, the constraint on the \mathbf{m}_X 's on the B tetrahedra can be expressed in terms of the fields on the surrounding A tetrahedra. On each B tetrahedron, one obtains a set of equations of the following general form:

$$\begin{aligned} \mathbf{m}_Y(\mathbf{R}_B) &= 0 \\ \implies \sum_{i=1}^4 \sum_{X \in \text{gs}} \sum_{\alpha} c_{i\alpha X} m_X^\alpha(\mathbf{R}_B + \mathbf{u}_i) &= 0, \end{aligned} \quad (19)$$

where, on the second line, the \mathbf{u}_i 's are the FCC lattice vectors connecting the center of each B tetrahedron to the centers of the four neighboring A tetrahedra. In this exact expression, the sum taken over the X irreps is performed over those X in the A tetrahedra that are not

constrained to vanish according to Eq. (18), with sum over α running over all components of the \mathbf{m}_X^α fields. The $c_{i\alpha X}$'s are constant (transformation) coefficients obtained by expressing the B tetrahedra \mathbf{m}_X fields in terms of those on the A tetrahedra. The specific value of these $c_{i\alpha X}$ can be worked out using the linear relations between the fields \mathbf{m}_X and the spins \mathbf{S} using Table II⁶.

The constraints on the \mathbf{m}_X^α prescribed by Eq. (19) can be expressed into a form reminiscent of Gauss's law by applying a coarse-graining procedure, i.e.

$$\begin{aligned} \sum_{i=1}^4 \sum_{X \in \text{gs}} \sum_{\alpha} c_{i\alpha X} m_X^\alpha(\mathbf{R}_B + \mathbf{u}_i) &= 0 \\ \xrightarrow{\text{coarse-grained}} \sum_{X \in \text{gs}} \sum_{\alpha} D_{\alpha X} m_X^\alpha &= 0, \end{aligned} \quad (20)$$

where $D_{\alpha X}$ are a generalized set of derivatives labeled by the irrep component upon which these are applied.

To derive such a continuum description, we assume, for each \mathbf{m}_X , the existence of some underlying smoothly varying field $\mathbf{m}_X(\mathbf{r})$ defined at all points in space (here we slightly abuse the notation to use \mathbf{m}_X to refer to both the irreps on the discrete lattice and the coarse-grained fields). We further suppose that if a smoothly varying field $\mathbf{m}_X(\mathbf{r})$ is evaluated at the center of an A tetrahedron, it takes the value of \mathbf{m}_X on that tetrahedron center. Then, assuming slow variations of the fields, we approximate $m_X^\alpha(\mathbf{R}_B - \mathbf{u}_i)$ in Eq. (19) by a low-order gradient expansion of $\mathbf{m}_X(\mathbf{r})$ about $\mathbf{r} = \mathbf{R}_B$. Keeping the lowest order terms in the resulting expansion of Eq. (19) establishes the effective Gauss's law(s) governing the long-wavelength fluctuations of the $\mathbf{m}_X(\mathbf{r})$ fields within the ground state.

Working through this procedure yields the following set of correspondences between the microscopic constraints on the B tetrahedra and the constraints on the derivatives of the coarse-grained fields:

⁵ The mutual constraint between the A and B tetrahedra can be seen more clearly by writing the four spins belonging to the B tetrahedron in terms of the values of the \mathbf{m}_X fields on the four surrounding A tetrahedra.

⁶ A spin \mathbf{S}_i shared by two adjacent A and B tetrahedra is written

in terms of the $\mathbf{m}(\mathbf{R}_B)$ of the B tetrahedra, i.e. $\mathbf{S}_i[\mathbf{m}(\mathbf{R}_B)]$. Then, using the definition of the $\mathbf{m}(\mathbf{R}_A)$ fields for the A tetrahedron provided in Table II, a relationship between the fields on the A and B tetrahedra is obtained.

$$m_{A_2} = 0 \implies m_{A_2} = -\frac{a_d}{\sqrt{3}} \sin \phi \nabla \cdot \mathbf{m}_{T_{1,+}} + \frac{a_d}{\sqrt{3}} \cos \phi \nabla \cdot \mathbf{m}_{T_{1,-}} = 0, \quad (21)$$

$$\begin{aligned} \mathbf{m}_E = 0 \implies \mathbf{m}_E = & \frac{a_d}{2\sqrt{3}} \cos \phi \left(\frac{2\partial_x m_{T_{1,+}}^x - \partial_y m_{T_{1,+}}^y - \partial_z m_{T_{1,+}}^z}{\sqrt{3}(\partial_y m_{T_{1,+}}^y - \partial_z m_{T_{1,+}}^z)} \right) + \frac{a_d}{2\sqrt{3}} \sin \phi \left(\frac{2\partial_x m_{T_{1,-}}^x - \partial_y m_{T_{1,-}}^y - \partial_z m_{T_{1,-}}^z}{\sqrt{3}(\partial_y m_{T_{1,-}}^y - \partial_z m_{T_{1,-}}^z)} \right) \\ & + \frac{a_d}{2\sqrt{3}} \left(\frac{\sqrt{3}(-\partial_y m_{T_2}^y + \partial_z m_{T_2}^z)}{2\partial_x m_{T_2}^x - \partial_y m_{T_2}^y - \partial_z m_{T_2}^z} \right) = 0, \end{aligned} \quad (22)$$

$$\mathbf{m}_{T_2} = 0 \implies \mathbf{m}_{T_2} = \frac{a_d}{2\sqrt{3}} \begin{pmatrix} 2\partial_x m_E^2 \\ -\sqrt{3}\partial_y m_E^1 - \partial_y m_E^2 \\ \sqrt{3}\partial_z m_E^1 - \partial_z m_E^2 \end{pmatrix} + \frac{a_d}{2} \cos \phi \nabla \times \mathbf{m}_{T_{1,+}} + \frac{a_d}{2} \sin \phi \nabla \times \mathbf{m}_{T_{1,-}} = 0, \quad (23)$$

$$\begin{aligned} \mathbf{m}_{T_{1,-}} = 0 \implies \mathbf{m}_{T_{1,-}} = & \frac{a_d}{\sqrt{3}} \cos \phi \nabla m_{A_2} + \frac{\sqrt{3}a_d}{2} \sin \phi \cos \phi \begin{pmatrix} \partial_y m_{T_{1,+}}^z + \partial_z m_{T_{1,+}}^y \\ \partial_z m_{T_{1,+}}^x + \partial_x m_{T_{1,+}}^z \\ \partial_x m_{T_{1,+}}^y + \partial_y m_{T_{1,+}}^x \end{pmatrix} \\ & + \frac{a_d}{2\sqrt{3}} \sin \phi \begin{pmatrix} 2\partial_x m_E^1 \\ -\partial_y m_E^1 + \sqrt{3}\partial_y m_E^2 \\ -\partial_z m_E^1 - \sqrt{3}\partial_z m_E^2 \end{pmatrix} + \frac{a_d}{2} \sin \phi \nabla \times \mathbf{m}_{T_2} = 0, \end{aligned} \quad (24)$$

$$\begin{aligned} \mathbf{m}_{T_{1,+}} = 0 \implies \mathbf{m}_{T_{1,+}} = & -\frac{a_d}{\sqrt{3}} \sin \phi \nabla m_{A_2} - \frac{\sqrt{3}a_d}{2} \sin \phi \cos \phi \begin{pmatrix} \partial_y m_{T_{1,-}}^z + \partial_z m_{T_{1,-}}^y \\ \partial_z m_{T_{1,-}}^x + \partial_x m_{T_{1,-}}^z \\ \partial_x m_{T_{1,-}}^y + \partial_y m_{T_{1,-}}^x \end{pmatrix} \\ & + \frac{a_d}{2\sqrt{3}} \cos \phi \begin{pmatrix} 2\partial_x m_E^1 \\ -\partial_y m_E^1 + \sqrt{3}\partial_y m_E^2 \\ -\partial_z m_E^1 - \sqrt{3}\partial_z m_E^2 \end{pmatrix} + \frac{a_d}{2} \cos \phi \nabla \times \mathbf{m}_{T_2} = 0. \end{aligned} \quad (25)$$

Here, a_d is the distance between two neighboring tetrahedron centers. We first give here the *full* irrep-dependence of the lowest-order gradient expansion of a given field \mathbf{m}_γ in terms of all the remaining \mathbf{m}_χ fields, *and not just* those that are frozen in the ground-state manifold.

In practice, Gauss's laws for a particular system are obtained by only considering the differential equations resulting from the frozen \mathbf{m}_γ fields on the left-hand sides of Eq. (21)-(25) while only keeping terms involving the fluctuating \mathbf{m}_χ fields on the right-hand sides. In the next subsection, we provide an example of this procedure for

the classical spin ice spin liquid.

C. The non-Kramers case

We start by considering the case of non-Kramers ions with their effective spin Hamiltonian for which the irrep analysis and inter-tetrahedra constraints take simpler forms. In this case, as discussed in Sec. II, $J_{z\pm} = 0$, so that $a_{T_{1,ip}} = 0$ (see Table III). As a consequence, the irreps $\mathbf{m}_{T_{1,i}}$ and $\mathbf{m}_{T_{1,p}}$ do not mix, hence $\phi = 0$ [see Eq. (12)]. The inter-tetrahedra constraints then take a rather compact form

$$m_{A_2} = 0 \implies m_{A_2} = \frac{a_d}{\sqrt{3}} \nabla \cdot \mathbf{m}_{T_{1,i}} = 0, \quad (26)$$

$$\mathbf{m}_E = 0 \implies \mathbf{m}_E = \frac{a_d}{2\sqrt{3}} \begin{pmatrix} 2\partial_x m_{T_{1,p}}^x - \partial_y m_{T_{1,p}}^y - \partial_z m_{T_{1,p}}^z \\ \sqrt{3}(\partial_y m_{T_{1,p}}^y - \partial_z m_{T_{1,p}}^z) \end{pmatrix} + \frac{a_d}{2\sqrt{3}} \begin{pmatrix} \sqrt{3}(-\partial_y m_{T_2}^y + \partial_z m_{T_2}^z) \\ 2\partial_x m_{T_2}^x - \partial_y m_{T_2}^y - \partial_z m_{T_2}^z \end{pmatrix} = 0, \quad (27)$$

$$\mathbf{m}_{T_2} = 0 \implies \mathbf{m}_{T_2} = \frac{a_d}{2\sqrt{3}} \begin{pmatrix} 2\partial_x m_E^2 \\ -\sqrt{3}\partial_y m_E^1 - \partial_y m_E^2 \\ \sqrt{3}\partial_z m_E^1 - \partial_z m_E^2 \end{pmatrix} + \frac{a_d}{2} \nabla \times \mathbf{m}_{T_{1,p}} = 0, \quad (28)$$

$$\mathbf{m}_{T_{1,i}} = 0 \implies \mathbf{m}_{T_{1,i}} = \frac{a_d}{\sqrt{3}} \nabla m_{A_2} = 0, \quad (29)$$

$$\mathbf{m}_{T_{1,p}} = 0 \implies \mathbf{m}_{T_{1,p}} = \frac{a_d}{2\sqrt{3}} \begin{pmatrix} 2\partial_x m_E^1 \\ -\partial_y m_E^1 + \sqrt{3}\partial_y m_E^2 \\ -\partial_z m_E^1 - \sqrt{3}\partial_z m_E^2 \end{pmatrix} + \frac{a_d}{2} \nabla \times \mathbf{m}_{T_2} = 0. \quad (30)$$

Before proceeding, we note that for the non-Kramers Hamiltonian, the local z spin degrees of freedom transform as (time-odd) magnetic dipoles while the local xy spin degrees of freedom transform as (time-even) magnetic quadrupoles [35]. This forbids a bilinear mixing of these degrees of freedom, imposing $J_{z\pm} = 0$. This restriction is further reflected in Eq. (26)-(30) where each constraint results in differential equations involving fields constructed by the local z spin degrees of freedom (the A_2 and the $T_{1,i}$ fields) *or* by the local xy spin degrees of freedom (the E , the $T_{1,p}$, and the T_2 fields), with those two sets being decoupled. This distinction allows us to further classify the constraints in Eq. (26)-(30) into two independent sets of constraints.

For illustration purposes, let us take Eq. (26) as an example to show how these field-theory constraints are derived. We label the four sublattice sites on the B tetrahedron to be 0, 1, 2, 3,, and find

$$m_{A_2} = S_0^z + S_1^z + S_2^z + S_3^z. \quad (31)$$

The B tetrahedron is joined with an A tetrahedron along the [111] cubic direction by the spin S_0 . We see that on the A tetrahedron, S_0^z can be expressed as linear combinations of \mathbf{m} fields on that A tetrahedron as

$$S_0^z = \frac{1}{4} (m_{A_2} + [111] \cdot \mathbf{m}_{T_{1,i}}). \quad (32)$$

Repeating a similar manipulation for the other spins $S_{1,2,3}$ results in the follow expression relating m_{A_2} on a B tetrahedron, $m_{A_2}(\mathbf{R}_B)$, to the neighboring four A

tetrahedra, namely

$$m_{A_2}(\mathbf{R}_B) = \frac{1}{4} \sum_i \left(m_{A_2}(\mathbf{R}_B + \mathbf{u}_i) + \frac{a_d}{\sqrt{3}} \hat{\mathbf{u}}_i \cdot \mathbf{m}_{T_{1,i}}(\mathbf{R}_B + \mathbf{u}_i) \right), \quad (33)$$

Then, applying the constraint $m_{A_2} = 0$ and taking the \mathbf{m}_X fields to the continuous limit, we obtain

$$m_{A_2} = 0 \implies \nabla \cdot \mathbf{m}_{T_{1,i}} = 0, \quad (34)$$

which gives Eq. (26). The other equations in Eqs. (21-25) and Eqs. (26-30) can be derived in the same fashion by considering the other \mathbf{m}_X fields on the left side of those equations one at a time, although the algebra is considerably more lengthy.

D. Step-by-step procedure for deriving Gauss's law

We now use the irreps and inter-tetrahedra constraints to identify the CSLs that the model supports for non-Kramers ions. We consider all combinations of coefficients a_X 's that can be consistently minimal with the a_Y 's simultaneously not minimal in the single-tetrahedron Hamiltonian. The procedure for constructing the field theory is then:

- *Step #0*: Compute the a_X coefficients for all irrep fields and identify all the minimum energy irreps for which $a_X = \mathcal{E}_0$ according to Eq. (15). This will ultimately allow us to determine the fields fluctuating in the ground state.

- *Step #1:* Then, identify all $\mathbf{m}_Y = 0$ as constrained by Eq. (18) which become frozen and are thermally depopulated in the limit $T \rightarrow 0$.
- *Step #2:* Then, identify all \mathbf{m}_X 's that are free to fluctuate.
- *Step #3:* Next, identify the constraints on the \mathbf{m}_X 's imposed by $\mathbf{m}_Y = 0$ frozen fields through the inter-tetrahedra relations Eqs. (21-25) for the Kramers ions or Eqs. (26-30), for the non-Kramers ions.
- *Step #4:* Finally, check that in the large- \mathcal{N} theory, the $a_X = \mathcal{E}_0$ parameters identified above yield low-energy flat bands reflecting a possible extensive ground-state degeneracy characteristic of a classical spin liquid phase. The number of flat band corresponds to the number of DOFs in the emergent electric fields minus the number of constraints.

In this procedure, steps #0 to #3 allow one to identify a set of constraints (Gauss's laws) for the allowed fluctuating fields, \mathbf{m}_X , of a given model. Step #4 then verifies that these constraints *may result* in a CSL by studying the degeneracy of the ground-state manifold in the large- \mathcal{N} limit. Subsequently, we performed CMC simulations (reported in Section VII) for the lattice Hamiltonian in Eq. (1) to find out which of the sets of parameters identified above as candidate CSLs are indeed such (for the $\mathcal{N} = 3$ model) down to the lowest temperature.

To illustrate further, let us discuss now a simple and concrete example to demonstrate how to execute the above protocol, considering the classical spin ice spin liquid. This spin liquid is a non-Kramers case so $a_{T_{1,p}} = 0$, and the irreps $\mathbf{m}_{T_{1,p}}$ and $\mathbf{m}_{T_{1,i}}$ do not mix. Following the procedure, we thus have:

- *Step #0:* For this choice of a_X parameters, we have that $\mathcal{E}_0 = a_{T_{1,i}}$ such that $a_{A_2}, a_E, a_{T_{1,p}}$ and $a_{T_2} > \mathcal{E}_0$.
- *Step #1:* $a_{T_{1,i}}$ is minimal and the others a_X are not (ref. Table. III) and, therefore, all other $\mathbf{m}_Y = 0$ for $Y = A_2, E, T_{1,p}$ and T_2 .
- *Step #2:* As stated just above, the only field able to thermally fluctuate in the present case is $\mathbf{m}_{T_{1,i}}$.
- *Step #3:* While $\mathbf{m}_{T_{1,i}}$ remains fluctuating, and despite a set of fields being frozen, the allowed spin patterns associated with the latter constrain $\mathbf{m}_{T_{1,i}}$. Indeed, according to Eq. (26), the field $\mathbf{m}_{T_{1,i}}$ is constrained by $m_{A_2} = 0 \implies \nabla \cdot \mathbf{m}_{T_{1,i}} = 0$. This is exactly the well-known emergent Maxwell's Gauss's law for classical spin ice [20, 28], with the charge-free condition imposed for the ground state configurations.
- *Step #4:* Lastly, the band structure for this model yields two low-energy flat bands reflecting the extensive degeneracy associated with this spin liquid. This is because the emergent electric field,

$\mathbf{m}_{T_{1,i}}$, has three DOFs, and there is one constraint, namely $m_{A_2} = 0$ (recalling that A_2 is a one-dimensional irrep; see Table II).

IV. CSLS FOR NON-KRAMERS SPINS

A. Identification of CSLs for non-Kramers spins

We are now ready to employ the methodology developed in Sec. III to systematically scan the whole parameter space $\{J_{zz}, J_{\pm}, J_{\pm\pm}, J_{z\pm}\}$ of the nearest-neighbor Hamiltonian in Eq. (1) without the single-ion anisotropy term in Eq. (3). In this section, we present all the CSLs identified in non-Kramers spin models. As discussed above, in this case $a_{T_{1,p}}$ vanishes, so $\mathbf{m}_{T_{1,p}}$ and $\mathbf{m}_{T_{1,i}}$ are the correct linear combinations of the T_d irreps in the diagonalized form of the single-tetrahedron Hamiltonian. Applying Step #3, we then use Eqs. (26-30) to derive the Gauss's laws. Following this procedure, we identified five distinct types of CSLs which we now proceed to discuss. The non-Kramers spin liquids are listed in Table I as CSL 1-5, and their location in the phase diagram is indicated in Fig. 2.

CSL 1. Single R1U1 (Spin ice): The first case is the well-known spin ice. While our model considers three-component spins rather than strictly Ising-like (one-component) spins, the ground state properties remain unchanged. In this case, the coefficient $a_{T_{1,i}}$ is minimal, and all the other coefficients are greater than $a_{T_{1,i}}$. The effective physics of this spin liquid was already analyzed as the simplest example of the inter-tetrahedra coarse-graining rule at the end of Sec. III C, Eqs. (26).

As shown there, a Gauss's law is obtained, given by

$$m_{A_2} = 0 \implies \nabla \cdot \mathbf{m}_{T_{1,i}} \equiv \nabla \cdot \mathbf{E}^{\text{ice}} = 0, \quad (35)$$

which is equivalent to the Maxwell U(1) Gauss's law. As is well-known for this regime, the charge (in some literature referred to as magnetic monopole) is measured by $m_{A_2} = S_1^z + S_2^z + S_3^z + S_4^z$, and imposes the microscopic 2-in-2-out "ice-rule" for the ground states [19, 29].

CSL 2. Double R1U1 (SL_{\perp}): The second CSL that we consider in the phase diagram arises when $a_{T_{1,p}}$ and a_{T_2} are simultaneously minimal, while the other a_Y 's are not. In this case, the vanishing (i.e. frozen out) field $\mathbf{m}_E = 0$ imposes constraints on the $\mathbf{m}_{T_{1,p}}$ and \mathbf{m}_{T_2} fluctuating fields, with the constraints given by Eq. (27). This can be written as two copies of a Maxwell U(1) Gauss's law:

$$\mathbf{m}_E = 0 \implies \nabla \cdot \mathbf{E}^A = 0 \text{ and } \nabla \cdot \mathbf{E}^B = 0, \quad (36)$$

where

$$\mathbf{E}^A = (2m_{T_{1,p}}^x, -m_{T_{1,p}}^y - \sqrt{3}m_{T_2}^y, \sqrt{3}m_{T_2}^z - m_{T_{1,p}}^z), \quad (37)$$

$$\mathbf{E}^B = (2m_{T_2}^x, \sqrt{3}m_{T_{1,p}}^y - m_{T_2}^y, -\sqrt{3}m_{T_{1,p}}^z - m_{T_2}^z). \quad (38)$$

This CSL was previously identified and studied in Ref. [64]. There, it was found that the system remains in a spin liquid state down to a low temperature and that the dipolar spin-spin correlations in that regime are indeed described by a double U(1) Gauss's law. At very low temperatures, a hidden order quadrupolar (spin nematic) develops in which the spins spontaneously select a particular axis in the local xy -plane along which they co-align. Nevertheless, the spin-spin correlations themselves remain algebraic.

CSL 3. Triple R1U1 (pHAF): In this case, $a_{\mathbb{T}_{1,p}}$, $a_{\mathbb{T}_{1,i}}$ and $a_{\mathbb{T}_2}$ are simultaneously minimal while the other ones are not. For these parameters, CSL 1 and CSL 2 become degenerate. As a consequence, this CSL is described by an emergent spin ice \times Double U(1) field. This gives rise to three copies of Maxwell U(1) Gauss's laws which can be written compactly as

$$\partial_i E_{ij}^{\text{pHAF}} = 0, \quad (39)$$

where \mathbf{E}^{pHAF} is a 3×3 matrix,

$$\mathbf{E}^{\text{pHAF}} = [(\mathbf{E}^{\text{ice}})^T, (\mathbf{E}^{\text{A}})^T, (\mathbf{E}^{\text{B}})^T]. \quad (40)$$

We note that this CSL 3 state corresponds to the so-called pseudo-Heisenberg AFM point in parameter space [64]. The set of interaction parameters for which this CSL is realized corresponds to a *local* Heisenberg antiferromagnetic model where $J_{\pm}/J_{zz} = -1/2$. Indeed, the above description of this CSL is consistent with the understanding that its thermodynamic properties are identical to that of the HAFM model [63, 82], but now for spins described in their local basis, hosting three copies of U(1) Maxwell Gauss's law, one for each component of \mathbf{S} . Consequently, the Gauss' law in Eq. (39) simply describes a vanishing moment in the local basis, where \mathbf{E}^{ice} corresponds to the local z -moment, while the remaining fields to the local xy -moment.

CSL 4. R1U1-R2U1 (\mathbf{R}_1 - $\mathbf{R}_2^{\mathbb{T}_1}$): In this case, $a_{\mathbb{E}}$, $a_{\mathbb{T}_{1,p}}$ and $a_{\mathbb{T}_{1,i}}$ are minimal, and the other $a_{\mathbb{V}}$'s are not. The constraints give two co-existing Gauss's laws,

$$m_{\mathbb{A}_2} = 0 \implies \nabla \cdot \mathbf{E}^{\text{ice}} = 0, \quad (41)$$

$$\mathbf{m}_{\mathbb{T}_2} = 0 \implies$$

$$\sqrt{3}\nabla \times \mathbf{m}_{\mathbb{T}_{1,p}} + \begin{pmatrix} 2\partial_x m_{\mathbb{E}}^2 \\ -\sqrt{3}\partial_y m_{\mathbb{E}}^1 - \partial_y m_{\mathbb{E}}^2 \\ \sqrt{3}\partial_z m_{\mathbb{E}}^1 - \partial_z m_{\mathbb{E}}^2 \end{pmatrix} = 0. \quad (42)$$

The first equation is the same Maxwell Gauss's law as for spin ice, whereas the second equation can be rewritten in a more compact form by introducing a rank-2 "electric field" $E_{ij}^{\mathbb{T}_1+\mathbb{E}}$ with off-diagonal anti-symmetric and diagonal traceless components, defined as

$$\mathbf{E}^{\mathbb{T}_1+\mathbb{E}} = \begin{pmatrix} 2m_{\mathbb{E}}^2 & \sqrt{3}m_{\mathbb{T}_{1,p}}^z & -\sqrt{3}m_{\mathbb{T}_{1,p}}^y \\ -\sqrt{3}m_{\mathbb{T}_{1,p}}^z & -\sqrt{3}m_{\mathbb{E}}^1 - m_{\mathbb{E}}^2 & \sqrt{3}m_{\mathbb{T}_{1,p}}^x \\ \sqrt{3}m_{\mathbb{T}_{1,p}}^y & -\sqrt{3}m_{\mathbb{T}_{1,p}}^x & \sqrt{3}m_{\mathbb{E}}^1 - m_{\mathbb{E}}^2 \end{pmatrix}. \quad (43)$$

Using this $\mathbf{E}^{\mathbb{T}_1+\mathbb{E}}$ rank-2 tensor, the following vector charge Gauss's law, i.e. a higher-rank Gauss's law, is obtained from Eq. (42):

$$\partial_i E_{ij}^{\mathbb{T}_1+\mathbb{E}} = 0. \quad (44)$$

We note that the higher-rank Gauss's law in Eq. (44) resembles that of a rank-2 U(1) gauge theory, but it is not the symmetric tensor version studied in Refs. [97, 98]. In particular, this CSL 4 is characterized by *infinitely many* multipole-charge conservation laws. Defining $\rho_j = \partial_i E_{ij}^{\mathbb{T}_1+\mathbb{E}}$, we obtain the following conserved quantities:

$$f(x+y+z)(\rho_1 + \rho_2 + \rho_3), \quad (45)$$

$$g(x-y-z)(\rho_1 - \rho_2 - \rho_3), \quad (46)$$

$$k(-x+y-z)(-\rho_1 + \rho_2 - \rho_3), \quad (47)$$

$$l(-x-y+z)(-\rho_1 - \rho_2 + \rho_3), \quad (48)$$

where $f(w)$, $g(w)$, $k(w)$, $l(w)$ are arbitrary polynomials of the argument w . As an example, if we define $w = x + y + z$, the dipole $w(\rho_1 + \rho_2 + \rho_3)$, quadrupole $w^2(\rho_1 + \rho_2 + \rho_3)$, etc., are all conserved along the [111] direction. Such multipole-charge conservation laws apply to the four [111] cubic crystalline directions.

This CSL 4, and also the next one discussed just below, CSL 5, was very recently identified and studied in Ref. [66]. This CSL is interesting in that it displays two distinct spin-liquidity regimes as a function of temperature. At intermediate temperature, the energy-degenerate \mathbb{E} and both \mathbb{T}_1 irreps are thermally populated, resulting in the so-called rank-1–rank-2 (\mathbf{R}_1 - \mathbf{R}_2) spin liquid in which two-fold and four-fold pinch points are observed in the spin-spin correlations in reciprocal space. At low temperatures, the model exhibits a thermal depopulation of the \mathbb{E} and the $\mathbb{T}_{1,p}$ irreps associated with an entropic selection of the $\mathbb{T}_{1,i}$, thus leading to a spin-ice-like CSL at the lowest temperatures. The phenomenology observed in this model is loosely reminiscent of the liquid-to-liquid transition in some molecular liquids such as phosphorous [99], sulfur [100], and silicon [101]. We note that the additional \mathbb{T}_1 superscript label for CSL 4 indicates that the rank-2 tensor field $\mathbf{E}^{\mathbb{T}_1+\mathbb{E}}$ has a $\mathbf{m}_{\mathbb{T}_{1,p}}$ field dependence whereas its dual, CSL 5, has a dependence upon the $\mathbf{m}_{\mathbb{T}_2}$ field, as is further discussed next.

CSL 5. R1U1-R2U1 (\mathbf{R}_1 - $\mathbf{R}_2^{\mathbb{T}_2}$): In this case, $a_{\mathbb{E}}$, $a_{\mathbb{T}_2}$ and $a_{\mathbb{T}_{1,i}}$ are at their minimal value while the other ones are not. This spin liquid is related to the CSL 4 above via a duality that corresponds to local $\pi/2$ rotation defined as

$$\begin{aligned} J_{\pm\pm} &\rightarrow -J_{\pm\pm}, \\ (S^x, S^y) &\rightarrow (-S^y, S^x), \end{aligned} \quad (49)$$

or, alternatively, $S_j^{\pm} \rightarrow \pm i S_j^{\pm}$. In terms of irreps, this duality implies $m_{\mathbb{E}}^1 \leftrightarrow m_{\mathbb{E}}^2$ and $\mathbf{m}_{\mathbb{T}_2} \leftrightarrow \mathbf{m}_{\mathbb{T}_{1,p}}$. Implementing these dualities on the rank-2 tensor $\mathbf{E}^{\mathbb{T}_1+\mathbb{E}}$, we obtain the

dual rank-2 tensor $\mathbf{E}^{\text{T}_2+\text{E}}$. Altogether, the Gauss's laws describing this CSL 5 are

$$\begin{aligned} m_{\text{A}_2} = 0 &\implies \nabla \cdot \mathbf{E}^{\text{ice}} = 0, \\ \mathbf{m}_{\text{T}_{1,\text{p}}} = 0 &\implies \partial_i E_{ij}^{\text{T}_2+\text{E}} = 0, \end{aligned} \quad (50)$$

where $\mathbf{E}^{\text{T}_2+\text{E}}$ is defined similarly as $\mathbf{E}^{\text{T}_1+\text{E}}$, but now, by making replacement $\mathbf{m}_{\text{T}_{1,\text{p}}} \rightarrow \mathbf{m}_{\text{T}_2}$ and $(m_E^1, m_E^2) \rightarrow (-m_E^2, m_E^1)$. Thanks to the duality (49), the thermodynamical properties of this CSL 5 are identical to those of CSL 4. However, the spin-spin correlations themselves are different [66]. Lastly, we note that the interaction coupling parametrization of the non-Kramers compound $\text{Tb}_2\text{Ti}_2\text{O}_7$ [14, 16] and its stoichiometric variant $\text{Tb}_{2+x}\text{Ti}_{2-x}\text{O}_{7+y}$ [102] falls in close proximity to the parametrization of this CSL. The authors in Ref. [66] pointed out that the proximity of these parameterizations to this CSL may be crucial in the understanding of the low-temperature behavior of this magnetic compound.

B. Summary of the non-Kramers spins Hamiltonian

To summarize, the non-Kramers spin model hosts five CSLs in total, listed in Table I. In the of $J_{\pm} - J_{\pm\pm} - J_{zz}$ phase diagram illustrated in Fig. 2. Only the spin ice (CSL 1) exists as a phase occupying a 3D volume in parameter space; all other CSLs sit on phase transition planes or lines separating long-range ordered phases. The spin ice phase takes the shape of a three-edged pyramid. The double U(1) CSL (CSL 2) occupies a plane attached to an edge of the pyramid. The CSLs 3, 4, 5 are located on the three edges of the pyramid defined by the spin ice phase, a feature further manifested by the fact that their respective Gauss's laws incorporate the Maxwell U(1) Gauss's law of spin ice.

Various interesting points on the phase diagram were previously studied in the literature. Obviously, the most intensively studied one is spin ice. Besides, the CSLs 2 and 3 and their double and triple U(1) Gauss's laws, respectively, have also been investigated in Ref. [64]. On the other hand, the $\text{R}_1\text{-R}_2^{\text{T}_1}$ CSL 4 was very recently studied in Ref. [66]. There, the Hamiltonian of that model was coined the name dipolar-quadrupolar-quadrupolar (DQQ) model because it is realized at the triple point where two long-range ordered quadrupolar phases meet the disordered spin ice (magnetic dipolar) phase discussed Refs. [35, 89]. The CSL 5 ($\text{R}_1\text{-R}_2^{\text{T}_2}$) is realized at the dual point of the DQQ model, referred to as DQQ* in Ref. [66], so these the CSL 4 and CSL 5 share identical thermodynamics.

We note that, although there are also three triple-phase-boundary points for the case where $J_{zz} < 0$ (See Fig 2), which have three degenerate a_{X} 's, *all of these* exhibit a finite-temperature phase transition into an ordered state as found from classical Monte Carlo simulations. We direct the reader to Sec. VIII for more details

on these other specific models that we refer to as ‘‘failed CSL candidates’’.

V. CSLS FOR KRAMERS SPINS

A. Identification of CSLs for Kramers spins

In this section, we discuss the case of the spin model for Kramers ions. In terms of the bilinear Hamiltonian in Eq. (1), Kramers spins allow for a nonzero $J_{z\pm}$ interaction. When rewriting the Hamiltonian in terms of the irreps as discussed in Sec. III A, an additional term coupling the two T_1 irreps, $\mathbf{m}_{\text{T}_{1,\text{p}}}$ and $\mathbf{m}_{\text{T}_{1,\text{i}}}$, is now allowed in Eq. (5). Again, this originates from the fact that both S_i^z and S_i^{\pm} are time-odd, transforming as real spin-1/2 operators, and are coupled in Eq. (1). As previously discussed, the interaction between $\mathbf{m}_{\text{T}_{1,\text{p}}}$ and $\mathbf{m}_{\text{T}_{1,\text{i}}}$ via $a_{\text{T}_{1,\text{ip}}}$ in Eq. (5), can be eliminated by a change of basis within the $\text{T}_{1,\text{i}}$ and $\text{T}_{1,\text{p}}$ sector, giving a new basis defined by the fields $\mathbf{m}_{\text{T}_{1,+}}$ and $\mathbf{m}_{\text{T}_{1,-}}$ which diagonalizes the Hamiltonian H_t . The inter-tetrahedra constraints are then modified to be expressed in terms of these new $\mathbf{m}_{\text{T}_{1,\pm}}$ fields. This is discussed in detail from Eq. (6) to Eq. (13). We now proceed to discuss the CSLs that arise when $J_{z\pm}$, or equivalently, when $a_{\text{T}_{1,\text{ip}}}$, is non-zero. As done above for the non-Kramers case, we apply the procedure discussed in Sec. III D with the inter-tetrahedra constraints of Eqs. (21-25) to systematically search for the CSLs that Kramers ions can exhibit on the pyrochlore lattice. For the Kramers Hamiltonian, we have found in total four different types of CSLs, which are discussed in detail below. These CSLs are listed in Table I as CSL 6-9, and their phase diagram is shown in Fig. 3. There are actually two phase diagrams, for $J_{z\pm} > 0$ and $J_{z\pm} < 0$ respectively, but the geometry of the two phase diagrams are identical as a consequence of an exact duality of the Kramers Hamiltonian associated to a change of sign in the $J_{z\pm}$ coupling [16] which we discuss in further detail below.

CSL 6. Scalar-vector-charge (SV) R_2U_1 CSL:

This CSL is stabilized when the parameters a_E , a_{T_2} , and $a_{\text{T}_{1,-}}$ are simultaneously minimal, that is when

$$\begin{aligned} J_{z\pm} &> 0, \\ J_{zz} &> -\frac{1}{\sqrt{2}}J_{z\pm}, \\ J_{\pm} &= \frac{1}{12} \left(J_{zz} + \sqrt{J_{zz}^2 + 24J_{z\pm}^2} \right), \\ J_{\pm\pm} &= \frac{1}{6} \left(J_{zz} + \sqrt{J_{zz}^2 + 24J_{z\pm}^2} \right). \end{aligned} \quad (51)$$

In the 3D phase diagram of fixed $J_{z\pm}$, these equations parametrize a line. The effective Gauss's law for this CSL has a scalar charge and a vector charge defined for

its rank-2, traceless electric field,

$$m_{A_2} = 0 \implies |\epsilon^{ijk}| \partial_i E_{jk}^{SV} = 0, \quad (52)$$

$$\mathbf{m}_{T_{1,+}} = 0 \implies \partial_i E_{ij}^{SV} = 0, \quad (53)$$

where

$$\mathbf{E}^{SV} = \begin{pmatrix} 2m_E^1 & \sqrt{3}m_{T_2}^z & -\sqrt{3}m_{T_2}^y \\ -\sqrt{3}m_{T_2}^z & -m_E^1 + \sqrt{3}m_E^2 & \sqrt{3}m_{T_2}^x \\ \sqrt{3}m_{T_2}^y & -\sqrt{3}m_{T_2}^x & -m_E^1 - \sqrt{3}m_E^2 \end{pmatrix} - 3 \sin \phi \begin{pmatrix} 0 & m_{T_{1,-}}^z & m_{T_{1,-}}^y \\ m_{T_{1,-}}^z & 0 & m_{T_{1,-}}^x \\ m_{T_{1,-}}^y & m_{T_{1,-}}^x & 0 \end{pmatrix}. \quad (54)$$

Here, $|\epsilon^{ijk}|$ is the absolute value of the Levi-Civita symbol. The Gauss's law does not exhibit continuous rotational symmetry due to the contraction with $|\epsilon^{ijk}|$, which is not a covariant tensor. The correlation $\langle E_{ij}^{SV}(\mathbf{q}) E_{kl}^{SV}(-\mathbf{q}) \rangle$ exhibits both pinch-lines and four-fold pinch points, similar features to those observed in the pinch-line spin liquid [65].

Defining $\rho_0 \equiv |\epsilon^{ijk}| \partial_i E_{jk}^{SV}$ and $\rho_i \equiv \partial_i E_{ij}^{SV}$, we identify the following infinitely many conservation laws:

$$f(x+y+z)(-\rho_0 + \rho_1 + \rho_2 + \rho_3), \quad (55)$$

$$g(x-y-z)(-\rho_0 + \rho_1 - \rho_2 - \rho_3), \quad (56)$$

$$k(-x+y-z)(-\rho_0 - \rho_1 + \rho_2 - \rho_3), \quad (57)$$

$$l(-x-y+z)(-\rho_0 - \rho_1 - \rho_2 + \rho_3). \quad (58)$$

As before, $f(w)$, $g(w)$, $k(w)$, $l(w)$ are arbitrary polynomials of the argument w . We note that this particular CSL has not been previously studied, therefore we identify this as a novel higher-rank CSL. However, it is crucial to note that this CSL is dual to the pinch-line spin liquid [65]. This duality implies that the Gauss's laws and gauge fields of these CSLs have the same form resulting in the observation of both pinch-lines and multifold pinch points in their correlation functions. Lastly, we note that, although a similar gauge field as that in Eq. (54) describing the low-temperature physics of the pinch-line spin liquid was identified in Ref. [65], the precise details of the Gauss's laws, the conserved quantities, and the gauge charges associated with it were not discussed therein.

CSL 7. SV R2U1* (Pinch-line spin liquid):

This CSL has the same degeneracy of minimal parameters as CSL 6: a_E , a_{T_2} , and $a_{T_{1,-}}$ which, in terms of spin exchange parameters, amount to the conditions

$$\begin{aligned} J_{z\pm} < 0, \quad J_{zz} > \frac{1}{\sqrt{2}} J_{z\pm}, \\ J_{\pm} &= \frac{1}{12} \left(J_{zz} + \sqrt{J_{zz}^2 + 24J_{z\pm}^2} \right), \\ J_{\pm\pm} &= \frac{1}{6} \left(J_{zz} + \sqrt{J_{zz}^2 + 24J_{z\pm}^2} \right). \end{aligned} \quad (59)$$

The corresponding emergent Gauss's laws have the same functional form as those of CSL 6. The low-temperature physics of both spin liquids are described by a rank-2 gauge field constraint by the Gauss's laws in Eq. (52) and Eq. (53). However, the precise definition of the $\mathbf{m}_{T_{1,-}}$ and therefore the gauge fields themselves are distinct. The CSLs 6 and 7 should therefore be considered as different. First, the microscopic Hamiltonian parameters defining the two CSLs are different. Second, in the phase diagram, the two CSLs do not directly connect to each other as they are separated by the limit of $J_{z\pm} = 0$, which corresponds to the distinct CSL 4. Nonetheless, CSL 6 and 7 are related by the duality [16, 58]

$$\begin{aligned} J_{z\pm} &\rightarrow -J_{z\pm}, \\ (S^x, S^y, S^z) &\rightarrow (-S^x, -S^y, S^z). \end{aligned} \quad (60)$$

More generally, this duality implies that the phase diagram boundaries between magnetic orders are identical after reversing the sign of $J_{z\pm}$, but the magnetic orders themselves are not identical on the two sides. This duality and the one of Eq. (49) are two different dualities for two different models. The duality in Eq. (49) only applies to the non-Kramers Hamiltonian and is not (on its own) a duality of the Kramers Hamiltonian. The former one for $J_{z\pm}$ in Eq. (60) only applies to the Kramers Hamiltonian while in the non-Kramers case, the consequential transformation on the xy components of the pseudospins in Eq. (49) amounts to a trivial reflection symmetry. This CSL 7 was studied in Ref. [65]. Here, our observation of an infinite number of conserved charges, the duality of Eq. (60), and also the overall structure of the phase diagram complement that of a previous study [65]. We provide in Section VII below numerical evidence for the persistence of the spin liquid behavior for this phase for distinct values of $J_{z\pm}$ down to the lowest temperatures.

CSL 8. Triple R1U1 (HAFM): The second to last CSL that we identify is the well-known Heisenberg antiferromagnet (HAFM) [13, 62, 63, 82]. This CSL corresponds to the point where the CSL 6 meets the AIAO phase with the a_E , a_{T_2} , $a_{T_{1,-}}$, and a_{A_2} interaction parameters all being minimal. The spin-spin interaction parameters for this CSL are parametrized as

$$\begin{aligned} J_{z\pm} > 0, \quad J_{zz} &= -\frac{1}{\sqrt{2}} |J_{z\pm}|, \\ J_{\pm} &= \frac{1}{2\sqrt{2}} |J_{z\pm}|, \quad J_{\pm\pm} = \frac{1}{\sqrt{2}} |J_{z\pm}|. \end{aligned} \quad (61)$$

This point corresponds to the isotropic $O(3)$ Heisenberg antiferromagnetic model in the global spin basis. The Gauss's law for this CSL are three copies of $U(1)$, written in a compact form as

$$m_{T_{1,+}} = 0 \implies \partial_i E_{ij}^{\text{HAF}} = 0, \quad (62)$$

where

$$E_{ij}^{\text{HAF}} = E_{ij}^{\text{SV}} - 2\delta_{ij}(\tan \phi)m_{A_2}. \quad (63)$$

We see here that the scalar m_{A_2} field adds exactly to the trace component to the otherwise traceless E_{ij}^{SV} rank-2 field such that E_{ij}^{HAF} acquires the full nine degrees-of-freedom associated to a 3×3 matrix. These DOFs correspond to the nine components of the degenerate m_X fields, whose trace is the m_{A_2} field, two diagonal traceless elements are the \mathbf{m}_E field, three off-diagonal anti-symmetric elements are the \mathbf{m}_{T_2} field, and three off-diagonal symmetric elements are the $\mathbf{m}_{T_{1,-}}$ field. Altogether, these nine degrees of freedom and the three Gauss's laws in Eq. (62) result in six degenerate low-energy flat bands describing the ground state manifold of this CSL [82].

CSL 9. Triple R1U1 (HAFM*): The last CSL for the Kramers Hamiltonian that we identify is dual to the HAFM CSL 8, with $J_{z\pm} < 0$ and parametrized as

$$\begin{aligned} J_{z\pm} < 0, \quad J_{zz} &= -\frac{1}{\sqrt{2}}|J_{z\pm}|, \\ J_{\pm} &= \frac{1}{2\sqrt{2}}|J_{z\pm}|, \quad J_{\pm\pm} = \frac{1}{\sqrt{2}}|J_{z\pm}|. \end{aligned} \quad (64)$$

Just as the CSL 6, this CSL has not been previously studied and we therefore identify it as a novel CSL. The emergent Gauss's law of this CSL is identical to that of the HAFM CSL. Nevertheless, this CSL should be considered a different CSL, as the dual of HAFM via Eq. (60). Indeed, the Hamiltonian for this CSL in the global spin basis is different from the HAFM as we further discuss in Appendix B. Moreover, for the HAFM* the $T_{1,-}$ irrep corresponds to the colinear ferromagnet meaning that a single tetrahedron in the ground-state configuration of this spin liquid can have a finite magnetization, as opposed to those in the regular HAFM.

B. Summary of the Kramers spin Hamiltonian

To summarize, the Hamiltonian for Kramers ions hosts a total of four CSLs, as listed in Table I. In this case, the CSLs 6 and 7 are dual to each other, and so are CSLs 8 and 9, with the two dual partners in each pair yielding identical thermodynamic properties (see Section VII). Similar to the non-Kramers, the CSLs identified in the Kramers Hamiltonian separate distinct long-range ordered phases where the CSL 8 (9) are realized at the phase boundary between four phases, namely the A_2 , the E, the $T_{1,-}$ and the T_2 phases, localized at the tip of a pyramid corresponding to an A_2 phase as shown in Fig. 3. On the other hand, the CSL 6 (7) is realized upon leaving these maximally-degenerated points by gapping out the A_2 phase, as shown in Fig. 3.

The classical spin liquids that we identified above constitute the complete list of classical spin liquids that

can be realized in Kramers and non-Kramers pyrochlores with only nearest-neighbor bilinear interactions. We reiterate that the present section and Section IV only discuss the non-Kramers and Kramers nearest-neighbor bilinear spin Hamiltonians, respectively, but do not consider the special case of dipolar-octupolar Kramers systems as this particular spin model has been exhaustively discussed in previous works [39, 41]. In the next section, we discuss how and in what circumstances these spin liquids are connected and transition from one to another and what the consequences for their respective gauge theory are as the exchange parameters $\{J_{zz}, J_{\pm}, J_{\pm\pm}, J_{z\pm}\}$ are tuned.

VI. CONNECTIVITY OF THE CLASSICAL SPIN LIQUIDS AND EVOLUTION OF THEIR EFFECTIVE GAUGE THEORIES

In this section, we discuss the overall landscape of the CSLs that the anisotropic bilinear spin Hamiltonian of Eq. (1) on the pyrochlore lattice harbors. A hierarchy structure exists for these CSLs: generally, the CSLs with more degrees-of-freedom (DOFs) of low-energy fluctuations (more components in the emergent electric field and fewer constraints) require more a_X 's [see Eq. (5)] to be degenerate. As a consequence, such CSLs live in a subspace of low dimension in $J_{\mu\nu}$ parameter space. Furthermore, the CSLs with more DOFs are often delimited by other CSLs with more constrained Gauss's laws – the latter typically arising from lifting up some of the a_X 's above that of the lowest degeneracy value.

For example, the CSL 3 (pHAF) is a CSL with 6 DOFs of low energy fluctuations. These DOFs stem from the degeneracy of the 3-dimensional irreps, yielding 9 components of the emergent gauge field, constrained by 3 Gauss's laws, resulting in the 6 DOFs. In particular, starting from the CSL 3 with the degenerate $T_{1,i}$, $T_{1,p}$, and T_2 irreps, by lifting the degeneracy of one of the irrep modes,

$$(a_{T_{1,i}}, a_{T_{1,p}}, a_{T_2}) \rightarrow (a_{T_{1,p}}, a_{T_2}),$$

we obtain the CSL 2 (Double U(1)). On the other hand, by lifting the degeneracy $(a_{T_{1,i}}, a_{T_{1,p}}, a_{T_2}) \rightarrow a_{T_{1,i}}$, we obtain the CSL 1 (i.e. spin ice).

Another example is the transformation from CSL 8 to CSL 6 (and similarly CSL 9 to CSL 7), which is effectuated by the following degeneracy lifting

$$(a_{A_2}, a_E, a_{T_{1,-}}, a_{T_2}) \rightarrow (a_E, a_{T_{1,-}}, a_{T_2}).$$

In these transitions, the resulting Gauss's laws for the CSL 6 (CSL 7) are obtained from the previous Gauss' laws for CSL 8 (CSL 9) by reducing the number of free components of the corresponding gauge field and/or introducing new constraints.

Let us now discuss the transitions between different CSLs in more detail. First, let us elaborate on an important fact about CSLs 6 and 7. As discussed in Sec. V,

the parameter space identified in Eq. (51) for each one of these CSLs corresponds to a 2D surface, with no symmetry-breaking phase transition detected in Monte Carlo simulations down to the lowest temperatures, as we shall discuss in Sec. VII below. At low temperatures, effective Gauss's laws are imposed on an emergent rank-2 field constructed in terms of the E , T_2 , and $T_{1,-}$ irreps. This is the case for any point in the parameter space characterizing these two CSLs. However, it is crucial to realize that, although the form of the effective gauge theory remains the same, the precise constituents of the rank-2 field expressed in terms of spins do differ. Such variation is captured by the dependence of the rank-2 tensor on the parameters $\{v_{i\pm}, v_{p\pm}\}$ that define the $T_{1,-}$ irrep [Eqs. (6,7)]. Indeed, by tuning the constituents of the rank-2 fields, we are also effectively tuning the definition of the charge in these spin liquids. Consequently, one may understand the 2D spin liquid manifolds as a continuous set of models where the $T_{1,\pm}$ of the low-energy emergent gauge fields are smoothly evolving as a function of $J_{z\pm}$, while the full gauge fields are constrained to fulfill a set of Gauss's laws.

Having discussed how the effective gauge theories describing the CSL 6 and the CSL 7 smoothly evolve as the microscopic Hamiltonian parameters are modified while keeping the system in one of these two CSLs, we now turn to consider how these two CSLs are connected to each other. Figure 5 illustrates a phase diagram where the region of stability of multiple CSLs is shown. There, we take J_{zz} and $J_{z\pm}$ to be free parameters while $(J_{\pm}, J_{\pm\pm})$ are fixed by Eq. (51). We first note that the two parameter spaces defining the CSL 6 and CSL 7 meet on the line defined by $\{J_{zz}, J_{\pm}, J_{\pm\pm}, J_{z\pm}\} = \{J, J/6, J/3, 0\}$ with $J > 0$. This line, shown as the white dashed line in Fig. 5, corresponds to the CSL 5 [66], where the rank-2 fields decompose into one rank-2 field and one rank-1 field, each fulfilling an independent Gauss's law. In particular, for the CSL 6, the gauge field \mathbf{E}^{SV} in Eq. (54) and the Gauss's laws in Eqs. (52)-(53) decompose into the rank-1 \mathbf{E}^{ice} and the rank-2 $\mathbf{E}^{\text{T}_{1+\text{E}}}$ electric fields constrained by the Gauss's laws in Eq. (50). Importantly, this is the limit of vanishing $J_{z\pm}$ which characterizes non-Kramers ions discussed in Sec. IV ⁷.

The other boundaries of the CSL 6 and 7 parameter spaces are located at $J_{zz} = -\left|\frac{1}{\sqrt{2}}J_{z\pm}\right|$ with $J_{z\pm}$ positive for the CSL 6 while it is negative for the CSL 7. These two boundaries correspond to the CSL 8 (for $J_{z\pm} > 0$), and CSL 9 (for $J_{z\pm} < 0$), respectively. These boundaries, marked by solid white lines in Fig. 5, separate the CSL 6 and 7 from the A_2 (all-in/all-out, AIAO) magnetically

ordered phase. As discussed at the beginning of this section, the CSLs 8 and 9, "viewed" as the boundary of CSLs 6 and 7 with the magnetically ordered A_2 phase, have a higher degeneracy. The CSL 8 and 9 are thus CSLs with a higher number of low-energy-fluctuating DOFs [Eq. (62)], and contain all of the fluctuating DOFs of the CSLs 6 and 7 [Eq. (52)], respectively.

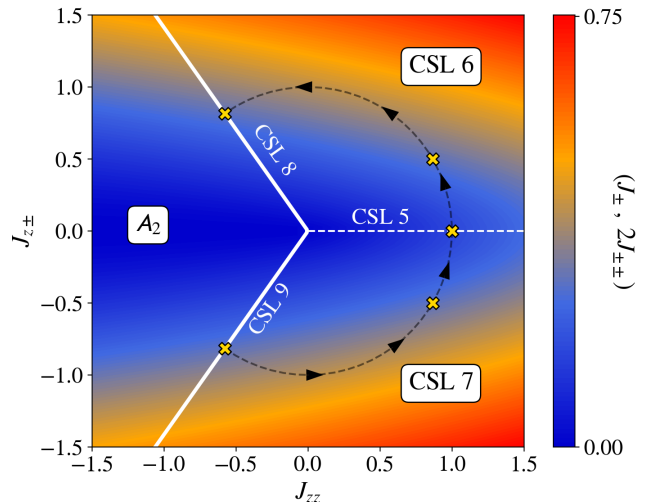


FIG. 5. Phase diagram illustrating how the classical spin liquids (CSLs) transition into/connect with each other. The diagram is drawn with respect to J_{zz} and $J_{z\pm}$, while J_{\pm} and $J_{\pm\pm}$ take values based on Eqs. (51,59). The upper right wedge is CSL 6, and lower right edge is CSL 7. The solid white lines, corresponding to CSL 8 and CSL 9, set the boundary between the spin liquid regime and the symmetry-breaking A_2 (AIAO) phase. The dashed white line separating CSL 6 and CSL 7 is the CSL 5. The reflection symmetry of the phase diagram about the x -axis is a consequence of the duality of Eq. (60). Lastly, the black dashed line indicates a way of tuning between the different spin liquids where the yellow crosses represent models for which the structure factors are shown in Fig. 6.

We have now discussed how the CSLs 6 and 7 display a smoothly varying definition of their electric field subject to the emergent Gauss's laws, and how they are connected to other CSLs on the boundary within the parameter space that define them. From an experimental context, such a change in the electric field can be exposed via the equal time polarized and unpolarized neutron structure factors which evolve as a function of the $J_{z\pm}$ and J_{zz} coupling parameters. Figure 6 illustrates the spin structure factor, unpolarized and polarized (spin flipping (SF) channel and non-spin flipping (NSF) channel) neutron structure factor in the $[hk0]$ plane for five different sets of parameters marked by yellow crosses in Fig. 5, which correspond to CSLs 9, 7, 5, 6, 8, in this respective order. The data illustrated here was obtained using a large- \mathcal{N} approximation which yields qualitatively similar results to those obtained with CMC simulations, except for the case with $J_{z\pm} = 0$ in the $T \rightarrow 0$ limit which displays disorder-by-disorder selection of a spin ice ground

⁷ Here we note that the interaction parameters corresponding to the CSL 5 in Fig. 5 are such that the ratio $J_{zz} : J_{\pm} : J_{\pm\pm} = 6 : 1 : 2$ is always fulfilled therefore identifying a 1D region as a function of J_{zz} as illustrated in Fig. 5. The evolution of these parameters on that boundary is given by the parametrization of the CSLs 6 and 7, Eqs. (51) and (59), while setting $J_{z\pm} = 0$.

state [66]. In this figure, and heretofore, we have considered an isotropic g tensor assuming that the fluctuations in all spin components are taken on equal footing in generating the neutron scattering structure factor [66, 103]. We refer the reader to Appendix D for the explicit definition of these correlation functions and for a short discussion regarding the choice of an isotropic g tensor used in these calculations. For the CSLs 5, 6 and 7, their effective gauge theories are characterized by an emergent Gauss’s law of a rank-2 electric field. The latter is responsible for the presence of four-fold pinch points in the correlation functions, besides the familiar two-fold pinch points, see Fig. 6 where white circles (squares) in the unpolarized neutron structure factor (polarized NSF channel) indicate the location of two-fold (four-fold) pinch points. Although these anisotropic features remain observable in the structure factors, the overall intensity distribution significantly changes reflecting the evolving nature of the gauge fields and their functional dependence on the parametrization used in Fig. 5.

Rather importantly, we note that the CSL 9 (HAFM*) also exhibits four-fold pinch points in its neutron structure factor at the Γ point, although its Gauss’s law is not associated with a higher-rank field. This four-fold pinch point is instead the consequence of the neutron (magnetic moment) scattering transverse projector [104], which is non-analytical at the Γ point, and *is not* caused by an emergent gauge structure of the model. We therefore note that, although the observation of four-fold pinch points is often a strong indication of an emergent higher-rank gauge theory, when observed at the Γ point, it is strictly neither a necessary nor a sufficient condition for the identification of such an underlying gauge theory⁸. This analysis therefore highlights the importance of studying the different accessible scattering channels to expose the anisotropic features associated with the realization of an emergent gauge theory, in addition to the development of an accompanying field theory analysis, as elaborated in Sec. III, to unequivocally identify a spin liquid phase and its underlying gauge theory.

As a final remark, we note that by combining the results summarized by the phase diagrams in Figs. 2, 3, and 5, we have established that *all* CSLs in Table I are *continuously* connected without having to pass through any conventional long-range ordered phase in the $\{J_{zz}, J_{\pm}, J_{\pm\pm}, J_{z\pm}\}$ parameter space. For example, from Figs. 3 and 5, we see that the Kramers CSLs 6, 7, 8 and 9, and the non-Kramers CSL 5 connect to each other.

⁸ We note that the CSL 5 exhibits a four-fold pinch point at (020) and symmetry-related points in its unpolarized neutron structure factors shown in the third row of Fig. 6. The spin structure factor of the same model, only shows two-fold pinch points at this q -point. These four-fold pinch points are produced by the combination of *two overlapping* two-fold pinch points, one coming from the rank-1 field (spin ice) and another from the rank-2 field (the \mathbf{E}^{T_2+E} field), and cannot be taken on their own as an indication of an emergent rank-2 gauge theory.

In addition, Fig. 2 shows that all the other non-Kramers CSLs connect to the CSL 5. The parameter space of the CSLs is delineated by a “main body” (i.e. the extended volume phase in parameter space that corresponds to the spin ice state) while various surfaces and lines define the other CSLs that extend out of the body.

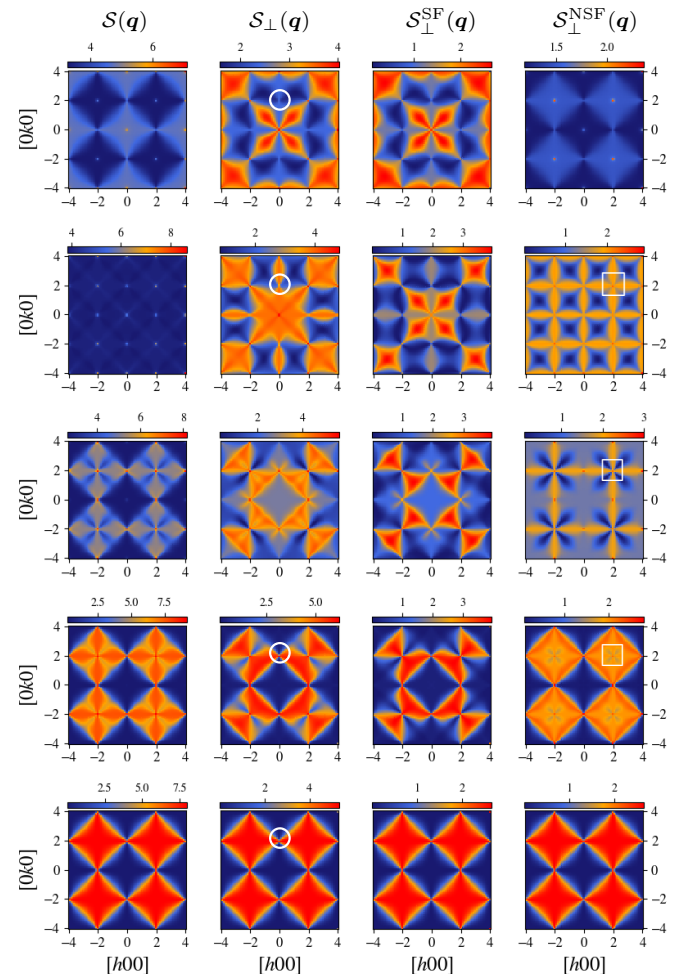


FIG. 6. Evolution of the spin structure factor (first column), neutron structure factor (second column), polarized neutron structure factor in the SF channel (third column), and polarized neutron structure factor in the NSF channel (fourth column) in the $[hk0]$ plane, computed using the large- \mathcal{N} approximation. In this figure, each row corresponds to a model parameterized by Eq. (51) labeled by the yellow crosses in Fig. 5 starting from the upmost row with the CSL 9 (HAFM*) and ending in the bottom row with the CSL 8 (HAFM), as indicated by the black circling arrows in Fig. 5. The white circles (squares) indicate the location of a two-fold (four-fold) pinch point. Definitions of each structure factor are given in Appendix D.

So far, we have presented an analysis of the gauge theories describing the low-temperature behavior of all possible CSLs realized by the generic anisotropic nearest-neighbor bilinear Hamiltonian on the pyrochlore lattice. Moreover, we have identified the features in reciprocal

space correlation functions that can allow to an identification of those CSLs. In the next section, we present a CMC numerical study of the heretofore unexplored new CSLs identified in this work, namely CSL 6 and CSL 9. In doing so, we compare the CMC results on these models with the predictions obtained from their respective gauge theory and the large- \mathcal{N} approximation.

VII. BEYOND LARGE- \mathcal{N} : THERMODYNAMICS AND STRUCTURE FACTORS FROM CLASSICAL MONTE CARLO

In this section, we present the results from CMC simulations of the two previously unidentified CSL 6 and CSL 9 discussed in Sec. V. Our simulations confirm that these unidentified CSLs do not exhibit magnetic order down to the lowest temperatures. The complete set of all possible CSLs of the most general nearest-neighbor bilinear Hamiltonian is presented in Table I. With the exception of CSL 1, all of these CSLs correspond to regions in parameter space where two or more symmetry-breaking ordered phases compete. We note, however, that the identification of a model at such boundaries is not a sufficient condition for a CSL to be realized and stable down to the lowest temperatures. Indeed, the models whose ground state manifold is characterized by a minimal A_2 and two additional irrep fields present a symmetry-breaking transition at low temperatures [94]. This transition is not predicted by the field theory which does not fully capture the $|\mathbf{S}|^2 = 1$ constraint of every spin. We discuss these special cases in Sec VIII below.

In the following, we present the thermodynamics of CSLs 6, 7, and 9 obtained via CMC simulations. The CSL 7 has already been discussed in Ref. [65], but its dual CSL 6, obtained via Eq. (60), has, to the best of our knowledge, not been discussed before. Although the two CSLs have the same effective theory, their structure factors display drastically different patterns. The same applies to CSL 9, which is dual to HAFM via the same equation (60). We show the specific heat and spin structure factor for the three CSLs marked in Fig. 5 by golden crosses, and whose structure factors are displayed in Fig. 6 in the first (uppermost row), second, and fourth rows.

For our simulations, we considered a system defined with an FCC unit cell composed of $4L^3$ spins with $L = 10$ and updated the system via a Gaussian spin-flip update [105], and an over-relaxation update [96, 106], in addition to averaging up to 10 independent CMC runs. We performed 8×10^4 thermalization sweeps and 2×10^5 measurement sweeps where we measured the energy, specific heat, and spin structure factors of the systems considered.

Figures 7 and 8 show the eigenvalue (bands) of the interaction matrix in momentum space, the specific heat, and the spin structure factors obtained for the parameters marked by the yellow crosses for the CSL 6 and CSL

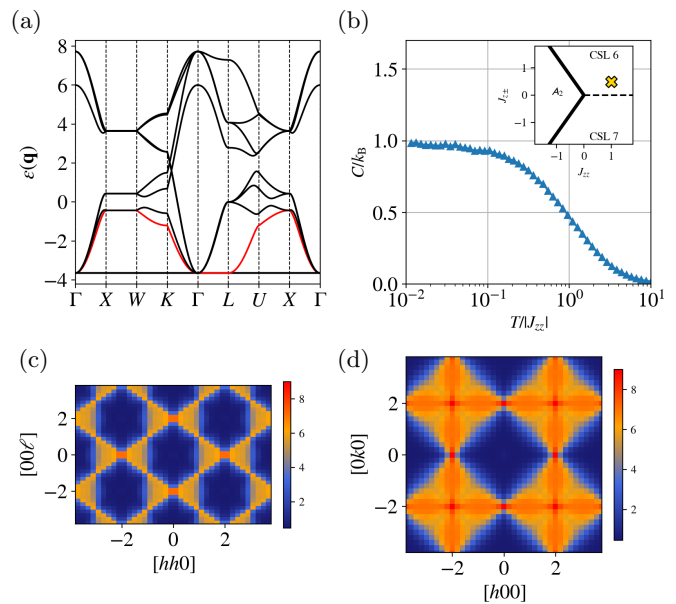


FIG. 7. (a) Diagonalized interaction matrix [Eq. (5)] bands in reciprocal space for CSL 6, using parameters $\{J_{zz}, J_{z\pm}\} = \{1, 0.5\}$ [Eq. (51)] where the lowest dispersive band is colored in red. There are four flat bands at the bottom in the spectrum. (b) Specific heat of the model, showing no sharp phase transitions from the paramagnetic phase down to the lowest temperature. The inset in this figure shows the location of the model in the phase diagram shown in Fig. 5. (c,d) spin structure factors in the $[hh\ell]$ and $[hk0]$ planes of the model.

7 in Fig. 5, respectively. As expected, and in agreement with the field analysis performed above, the band structure of the corresponding interaction matrices for these systems host four low-energy flat bands in their spectra (resulting from the 8 degrees of freedom and 4 constraints given by the Gauss's laws), see panel Figs. 7(a) and 8(a). The resemblance between the band structure of these two models is a consequence of the duality of the Hamiltonian [Eq. (1)] via Eq. (60). Neither model shows a sign of a thermodynamic phase transition, as indicated by the smooth evolution of the specific heat of both systems, see Fig. 7(b) and Fig. 8(b). The spin structure factors for both systems are shown in Fig. 7(c)-(d) and Fig. 8(c)-(d) for the $[hh\ell]$ and $[hk0]$ reciprocal space planes, respectively, showing excellent agreement with the predictions obtained via large- \mathcal{N} in Fig. 6.

In addition to the multifold pinch point anisotropies, we note that a distinctive feature in the correlation functions of CSL 7 is the observation of pinch lines, which can be observed in Fig. 8(c) along the $[111]$ and symmetry-related directions. In a large- \mathcal{N} theory, these features are produced by a dispersive band which, along the $[111]$ direction, becomes degenerate with the low-energy flat bands, see the first dispersive band marked in red in

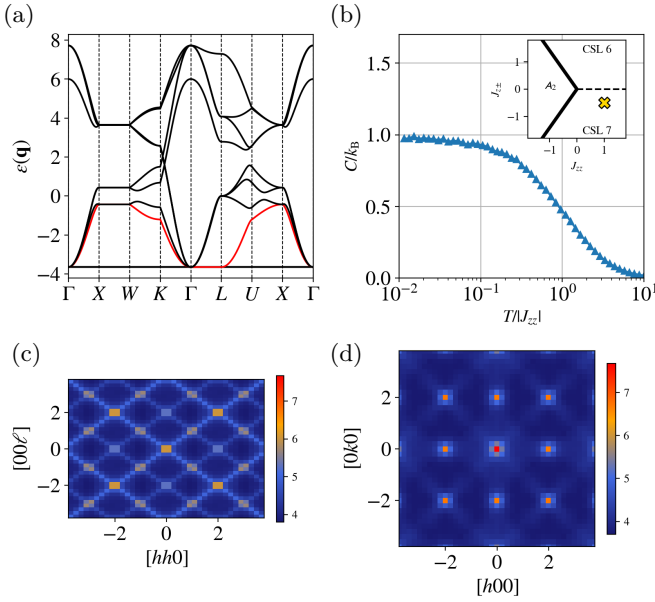


FIG. 8. (a) Diagonalized interaction matrix [Eq. (5)] band in reciprocal space for CSL 7, using parameters $\{J_{zz}, J_{z\pm}\} = \{1, -0.5\}$ [Eq. (59)] where the first dispersive band is colored in red. The spectrum is identical to Fig. 7 due to the duality of Eq. (60) between the two models. (b) Specific heat of the model, showing no sharp phase transitions from the paramagnetic phase down to the lowest temperature. The inset in this figure shows the precise location of the model in the phase diagram shown in Fig. 5. (c,d) spin structure factors in the $[hh\ell]$ and $[hk0]$ planes of the model. Although CSL 6 and CSL 7 are dual to each other, their spin structure factor is different. We note that the spin structure factor shown in panel (d) resembles the one predicted by SCGA in Fig. 6, where high-intensity signals are observed at the Γ , $[220]$, and $[200]$ points.

Fig. 7(a) and Fig. 8(a)⁹. Reference [65] noted that for the CSL 7 singular features (i.e. pinch points) in the reciprocal space correlation function are observed along the location of the pinch line in reciprocal space. In particular, four-fold pinch points can be observed at the intersection of multiple pinch lines. Given that the CSL 6 is dual to the CSL 7, pinch lines should naively be observed in the structure factor of CSL 6. Although it is not immediately clear from the structure factors in Fig. 7(c) and (d) where

⁹ The reason behind the observation of the pinch-lines in reciprocal space can be tracked to the degeneracy of the low-energy modes in reciprocal space. In the $T \rightarrow 0$ limit, the spin correlation functions obtained via SCGA is mainly determined by the contributions of the eigenmodes with the smallest eigenvalue. All others become negligible in the $T \rightarrow 0$ limit. In reciprocal space, the pinch-lines are observed for \mathbf{q} -points where a dispersive eigenmodes become degenerate with the low-energy modes. This leads to an enhanced intensity along these directions and therefore the observation of pinch lines.

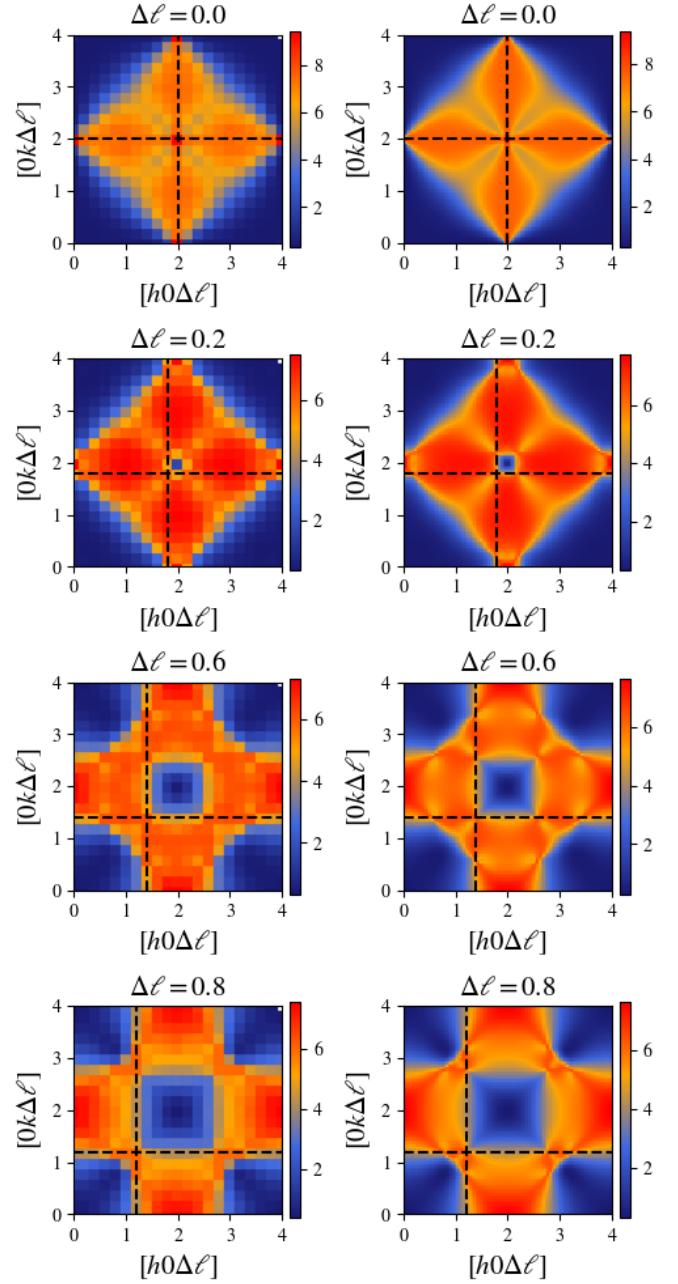


FIG. 9. Spin structure factors obtained via classical Monte Carlo simulations at $T = 0.03|J_{zz}|$ (left column) and large- \mathcal{N} approximation in the $T \rightarrow 0$ limit (right column) for the CSL 6 at various reciprocal plane cuts $[hk\Delta\ell]$, where the value of $\Delta\ell$ is specified at the top of each panel. Here, the black dashed lines are drawn at $h = 2 - \Delta\ell$ and $k = 2 - \Delta\ell$. The intersection of these lines marks the $\Delta\ell \times [11\bar{1}]$ direction which tracks the location of the pinch lines where two-fold pinch points are observed.

these features appear, we may track the location of the pinch lines by studying the spin structure factor in the vicinity of a four-fold pinch point. Figure 9 illustrates the spin structure factor for the CSL 6 in the $[hk\Delta\ell]$ plane for

increasing values of $\Delta\ell$ obtained via CMC and the large- \mathcal{N} method (see Appendix E) where the intersection of the black dashed lines tracks the location of one of the four pinch lines intersecting at the $[220]$ point. We note that, in both CMC and large- \mathcal{N} , as $\Delta\ell$ is increased, the four-fold pinch point (in the $[hk\Delta\ell]$ plane with $\Delta\ell = 0$) splits into four two-fold pinch points. The location of the two-fold pinch points with respect to the four-fold pinch point is consistent with a vector $\mathbf{q} = [\Delta\ell, \Delta\ell, \Delta\ell]$ and symmetry-related directions, corresponding to \mathbf{q} vectors where pinch lines are observed.

Lastly, we present in Fig. 10 the CMC results for CSL 9 corresponding to the dual HAFM model, HAFM*, which is CSL 8. This model presents the same functional form of the energy bands as the regular HAFM where the six low-energy bands of the interaction matrix are flat; see Fig. 10(a). Furthermore, and as found for the HAFM [62], the specific heat of this model presents no sign of symmetry-breaking transition down to the lowest temperatures where it plateaus to a value around the theoretical value $3/4$ [62, 63]. As in the HAFM, the spin structure factor of the HAFM* exhibits two-fold pinch points, as seen in the $[hk0]$ scattering plane both in CMC, and as predicted by large- \mathcal{N} . We further note that the structure factor of the HAFM* appears as an intensity-inverted version of that of the HAFM. In other words, the regions of high intensity in the spin structure factor of one model correspond to regions of low intensity in the dual model. This inversion is associated with the precise constraint acting in the ground-state manifold. For the HAFM, this constraint translates to a vanishing single-tetrahedron magnetization (which implies vanishing correlations around the Γ points). On the other hand, for the HAFM*, this constraint allows for a ferromagnetic configuration in the ground-state manifold (which results in a finite intensity at the Γ points) and forbids the antiferromagnetic configurations with a non-vanishing $T_{1,+}$ components.

VIII. THE FAILED CSL CANDIDATES

In this section, we briefly discuss the failed CSL candidates that sit on the boundaries between three magnetically ordered phases but yet present a symmetry-breaking transition at low temperatures. So far we have provided a list of the CSLs stable down to the lowest temperatures and therefore lack any type of conventional symmetry-breaking transition. In the large- \mathcal{N} approximation, a CSL is realized whenever the lowest band (or bands) of the interaction matrix is flat, resulting in an extensive degeneracy in the ground states. The extensive degeneracy associated with low-energy flat bands in the large- \mathcal{N} approximation, however, does not impede the onset of an order-by-disorder selection of a symmetry-breaking spin configuration. Such entropically driven selection mechanisms are typically described by high-order terms in the free energy which are not captured by the

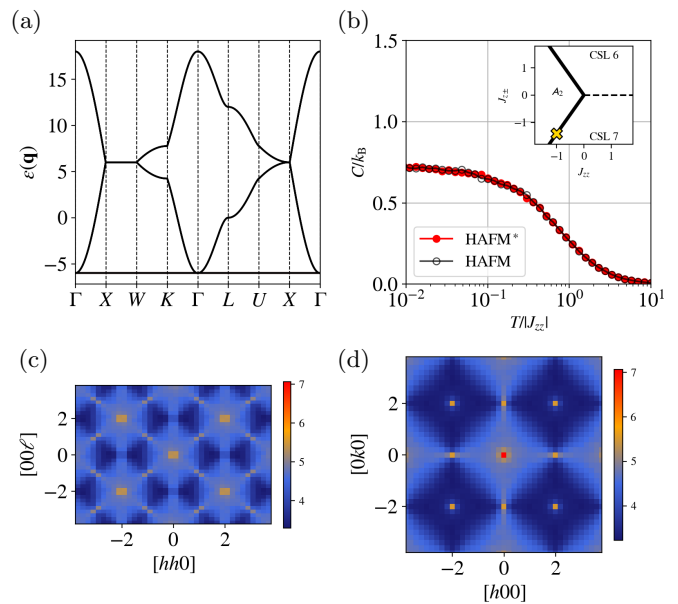


FIG. 10. (a) Interaction matrix bands, (b) specific heat, and structure factors in the $[hh\ell]$ (c) and $[hk0]$ (d) planes of the CSL9, the HAFM* model. (a) Diagonalized interaction matrix [Eq. (5)] band in reciprocal space for CSL 9 (HAFM*), using parameters $\{J_{zz}, J_{\pm}, J_{\pm\pm}, J_{z\pm}\} = \{-1.0, 0.5, 1, -\sqrt{2}\}$. There are six flat bands at the bottom of the spectrum and the dispersive bands are three-fold degenerate. The spectrum is identical to that of CSL 8 (HAFM) due to the duality of Eq. (60) between the two models. (b) Specific heat of the HAFM* and HAFM model, showing no sharp phase transitions in the paramagnetic phase down to the lowest temperature. The inset in this figure shows the precise location of the model in the phase diagram shown in Fig. 5. (c,d) neutron structure factors in the $[hh\ell]$ and $[hk0]$ planes of the model. Although CSL 8 and CSL 9 are dual to each other, their spin structure factor is different.

large- \mathcal{N} approximation [66]. Consequently, the stability of a CSL must be ascertained using CMC.

It turns out that, broadly speaking, these models are located at the three edges of the green pyramid of the A_2 phase (all-in-all-out magnetic order) Fig. 2(a) and Fig. 3 for the non-Kramers and Kramers Hamiltonian, respectively. These edges correspond to models in parameter space where three a_X are minimal, with the constraint that one of these minimal fields must be the A_2 field. As a shorthand notation, we refer to the models defined on these edges by the minimal irreps describing their ground states, namely, $A_2 \oplus T_{1,p} \oplus T_2$ (where the a_{A_2} , $a_{T_{1,p}}$, and a_{T_2} are minimal) [94], $A_2 \oplus E \oplus T_2$ (where the a_{A_2} , a_{T_E} , and a_{T_2} are minimal), and $A_2 \oplus E \oplus T_{1,p}$ (where the a_{A_2} , a_E , and $a_{T_{1,p}}$ are minimal) for the non-Kramers case. For the Kramers case, we use the same labeling but replace the $T_{1,p}$ field by $T_{1,-}$ field.

An analysis of the large- \mathcal{N} interaction matrix bands for the non-Kramers Hamiltonian models reveals that

the $A_2 \oplus T_{1,p} \oplus T_2$ model possesses four low-energy flat bands in its interaction matrix spectrum, whereas both the $A_2 \oplus E \oplus T_2$ and the $A_2 \oplus E \oplus T_{1,p}$ models yield two low-energy flat bands. On the other hand, for the Kramers models, both the $A_2 \oplus T_{1,-} \oplus T_2$ model and the $A_2 \oplus E \oplus T_2$ yield two low-energy flat bands, while the $A_2 \oplus E \oplus T_{1,-}$ has no flat bands in its interaction matrix spectrum. As previously mentioned, all of these models (with the exception of the $A_2 \oplus E \oplus T_{1,-}$ Kramers model) would have been predicted to be a CSL according to the large- \mathcal{N} analysis. However, a detailed analysis of CMC simulation data for these two models reveals that all of them undergo a symmetry-breaking phase transition at low temperatures (not shown in this paper). We leave the study of details of these failed CSL candidates for future work.

Lastly, we note that the CSLs listed in Table I and the failed CSL candidates discussed in this section constitute all the triple-phase boundary regions (with the exception of the CSL 1 (spin ice) and the CSL 2 (SL_{\perp}) phases) in the interaction parameter space $\{J_{zz}, J_{\pm}, J_{\pm\pm}, J_{z\pm}\}$ of the most generic nearest-neighbor Hamiltonian in the pyrochlore lattice. In a similar spirit, we also examined all boundaries separating two magnetic ordered phases, with the only CSL that we discovered being the CSL 2 that lives on the boundary of $T_{1,p}$ and T_2 magnetic orders. We thus have exhausted all potential parameter spaces supporting CSLs, and the list of CSLs for this general nearest-neighbor pyrochlore anisotropic spin Hamiltonian is thus complete.

IX. DISCUSSION AND CONCLUSION

Our work provides a comprehensive atlas of the CSLs that are realized on the pyrochlore lattice and wherein we have developed a theory of inter-tetrahedra constraints in terms of irreducible representation fields. In doing so, we identified the parameter spaces parameterizing all possible CSLs for the nearest-neighbor anisotropic spin Hamiltonian on the pyrochlore lattice. We have constructed effective gauge field theories for these CSLs and have explained how the CSLs are connected or transform into each other. Our results, summarized in Table I and Figs. 2, 3, 5, include nine distinct spin liquids described by various effective long-wavelength theories characterized by the emergence of energetically imposed Gauss-like law constraints. In aiming to obtain support for the field theory picture and to understand these systems quantitatively at the microscopic level, we also performed large- \mathcal{N} self-consistent Gaussian approximation (SCGA) and classical Monte Carlo (CMC) simulations.

Within the spin-spin couplings arising in the Hamiltonian of Eq. (1), the list of CSLs on the pyrochlore lattice is *exhaustive*. Referring to Figs. 2, 3, one notes that we have scanned all boundaries of two and three long-range ordered phases as well as the classically disordered spin ice phase. Therefore, we are confident that

there remain no other CSLs to be discovered in the phase diagram. By following our methodology to implement inter-tetrahedra constraints, and using CMC simulations, it would be straightforward to discover CSLs hosted by other anisotropic pyrochlore Hamiltonians. For example, one could consider other couplings such as the single-ion anisotropy term D in Eq. (3) and long-range dipole-dipole interactions, as long as the long-range ordered phase considered have a $\mathbf{q} = 0$ propagation vector. Extending our theory to CSLs stabilized by interactions beyond nearest neighbors [107, 108] as well as the breathing pyrochlore model [109] would also be an interesting line of study to pursue.

In this work, we have identified two new spin liquid phases and provide a full list of the possible CSLs in Table I. Specifically, these are the CSL 6 (as scalar-vector-charge R2U1, or SV R2U1), which is dual to the pinch-line spin liquid, and the CSL 9 as a dual to the well-known Heisenberg pyrochlore antiferromagnet (HAFM*). Although these two are dual to previously discovered CSLs, their spin couplings, ground-state manifold, and, consequently, their explicit effective gauge fields and associated structure factors are entirely different. The physical implications of the infinitely many charge-conservation laws for CSLs 6 and 7 that we noted in the present work is another interesting topic awaiting further study.

From the work presented here, we now have in hand a comprehensive overview of all the CSLs on the pyrochlore lattice and how these transform into each other as a consequence of modifying the lowest degenerate irreps by varying the anisotropic bilinear spin-spin couplings. Such insight is crucial for understanding the exotic physics of anisotropic spin models on the pyrochlore lattice, especially for materials that happen to be finding themselves near the phase boundaries of pseudospin long-range order [15, 56, 57, 76–78]. Our result provides crucial information for guiding the ultimate construction of a similar atlas for the quantum model, for example by exploring the vicinity of the CSL parameter spaces identified in this work, akin to what has been done in Ref. [66, 110]. Our atlas of CSLs on the pyrochlore lattice with nearest-neighbor couplings is a crucial step toward a complete understanding of one of the most representative frustrated magnetic systems.

ACKNOWLEDGMENTS

The authors acknowledge useful discussions with Ludovic Jaubert, Nic Shannon, Roderich Moessner, Yasir Iqbal, Rajiv Singh, Jaan Oitma Johannes Reuther, Andriy Nevidomskyy, Kristian Chung, and Matthias Vojta. D. L.-G. acknowledges financial support from the DFG through the Hallwachs-Röntgen Postdoc Program of the Würzburg-Dresden Cluster of Excellence on Complexity and Topology in Quantum Matter – *ct.qmat* (EXC 2147, project-id 390858490) and through SFB 1143 (project-id

247310070). H.Y. acknowledges the 2024 Toyota Riken Scholar Program from the Toyota Physical and Chemical Research Institute, and the Grant-in-Aid for Research Activity Start-up from Japan Society for the Promotion of Science (Grant No. 24K22856). The work at the University of Waterloo was supported by the NSERC of Canada and the Canada Research Chair (Tier 1, M.J.P.G.) program.

Appendix A: Local coordinates

In this appendix, we provide the convention that we follow for the local x and local z direction of the A tetrahedra shown in Fig. 1. The remaining local y directions are obtained via the cross-product of these two.

$$\mathbf{x}_0 = \frac{1}{\sqrt{6}}(-2, 1, 1), \quad (\text{A1})$$

$$\mathbf{x}_1 = \frac{1}{\sqrt{6}}(-2, -1, -1), \quad (\text{A2})$$

$$\mathbf{x}_2 = \frac{1}{\sqrt{6}}(2, 1, -1), \quad (\text{A3})$$

$$\mathbf{x}_3 = \frac{1}{\sqrt{6}}(2, -1, 1), \quad (\text{A4})$$

and

$$\mathbf{z}_0 = \frac{1}{\sqrt{3}}(1, 1, 1), \quad (\text{A5})$$

$$\mathbf{z}_1 = \frac{1}{\sqrt{3}}(1, -1, -1), \quad (\text{A6})$$

$$\mathbf{z}_2 = \frac{1}{\sqrt{3}}(-1, 1, -1), \quad (\text{A7})$$

$$\mathbf{z}_3 = \frac{1}{\sqrt{3}}(-1, -1, 1). \quad (\text{A8})$$

Appendix B: Hamiltonian in the “spin vector basis” and in the global basis

In this appendix, we provide an alternative basis for the general bilinear nearest-neighbor Hamiltonian in the pyrochlore lattice in Eq. (1) [55]. Doing so will further emphasize how the form of the spin Hamiltonian appears significantly different when considering the dual forms discussed above. The Hamiltonian can be parametrized in what we refer to as a “spin vector interaction” basis (SVI) basis with Heisenberg J , local Ising J_{Ising} , pseudo-dipole J_{PD} , and Dzyaloshinskii-Moriya (DM) J_{DM} interactions [55, 86]. In this SVI basis, the Hamiltonian in Eq (1) reads

$$\mathcal{H} = \mathcal{H}_{\text{Heis}} + \mathcal{H}_{\text{Ising}} + \mathcal{H}_{\text{PD}} + \mathcal{H}_{\text{DM}} \quad (\text{B1})$$

$$\mathcal{H}_{\text{Heis}} = J \sum_{\langle ij \rangle} \mathbf{S}_i \cdot \mathbf{S}_j \quad (\text{B2})$$

$$\mathcal{H}_{zz} = J_{\text{Ising}} \sum_{\langle ij \rangle} (\mathbf{S}_i \cdot \mathbf{z}_i) (\mathbf{S}_j \cdot \mathbf{z}_j) \quad (\text{B3})$$

$$\mathcal{H}_{\text{PD}} = J_{\text{PD}} \sum_{\langle ij \rangle} (\mathbf{S}_i \cdot \mathbf{r}_{ij}) (\mathbf{r}_{ij} \cdot \mathbf{S}_j) \quad (\text{B4})$$

$$\mathcal{H}_{\text{DM}} = J_{\text{DM}} \sum_{\langle ij \rangle} \mathbf{d}_{ij} \cdot (\mathbf{S}_i \times \mathbf{S}_j), \quad (\text{B5})$$

where the spins \mathbf{S}_i are here defined in the global Cartesian basis, \mathbf{z}_i is the local- z (cubic [111]) direction at the i th lattice site, \mathbf{r}_{ij} is the separation vector between lattices sites i and j , and \mathbf{d}_{ij} labels the direct DM vectors

$$\mathbf{d}_{03} = (-1, 1, 0), \quad \mathbf{d}_{02} = (1, 0, -1), \quad (\text{B6})$$

$$\mathbf{d}_{01} = (0, -1, 1), \quad \mathbf{d}_{32} = (0, 1, 1), \quad (\text{B7})$$

$$\mathbf{d}_{31} = (-1, 0, -1), \quad \mathbf{d}_{21} = (1, 1, 0). \quad (\text{B8})$$

as defined in Ref. [111]. The relation between the interaction parameters basis $\{J_{zz}, J_{\pm}, J_{\pm\pm}, J_{z\pm}\}$ and the above $\{J, J_{\text{Ising}}, J_{\text{PD}}, J_{\text{DM}}\}$ basis yields

$$J = 2(J_{\pm} + J_{\pm\pm}), \quad (\text{B9})$$

$$J_{\text{Ising}} = -10J_{\pm} - 2J_{\pm\pm} + 4\sqrt{2}J_{z\pm} + J_{zz}, \quad (\text{B10})$$

$$J_{\text{PD}} = -4(2J_{\pm} + J_{\pm\pm} - \sqrt{2}J_{z\pm}), \quad (\text{B11})$$

$$J_{\text{DM}} = -4J_{\pm} + \sqrt{2}J_{z\pm}. \quad (\text{B12})$$

Consider now the duality between CSL 8 and CSL 9 that is generated upon the change of sign of $J_{z\pm}$. In SVI basis, the former is simply an antiferromagnetic Heisenberg model, namely $\{J, J_{\text{Ising}}, J_{\text{PD}}, J_{\text{DM}}\} = \{\frac{3}{\sqrt{2}}J_{z\pm}, 0, 0, 0\}$, while the CSL 9 is a model where all parameters in the SVI basis are non-vanishing, i.e. $\{J, J_{\text{Ising}}, J_{\text{PD}}, J_{\text{DM}}\} = \{-\frac{3}{\sqrt{2}}J_{z\pm}, 8\sqrt{2}J_{z\pm}, 8\sqrt{2}J_{z\pm}, 2\sqrt{2}J_{z\pm}\}$.

We further note that, in addition to the local basis, i.e. $\{J_{zz}, J_{\pm}, J_{\pm\pm}, J_{z\pm}\}$, and the SVI basis, $\{J, J_{\text{Ising}}, J_{\text{PD}}, J_{\text{DM}}\}$, a global parameter basis, namely $\{J_1, J_2, J_3, J_4\}$ is also extensively used in the literature. In the global basis, the spin components are expressed in global Cartesian coordinates, and the spin Hamiltonian takes the form

$$H_{\text{ex}} = \sum_{\langle ij \rangle} \mathbf{S}_i \cdot \mathcal{J}_{ij} \cdot \mathbf{S}_j, \quad (\text{B13})$$

where the exchange matrix \mathcal{J}_{ij} couples the spins at the i and j sites. For instance, for sublattices 0 and 1, this exchange matrix takes the form

$$\mathcal{J}_{01} = \begin{pmatrix} J_2 & J_4 & J_4 \\ -J_4 & J_1 & J_3 \\ -J_4 & J_3 & J_1 \end{pmatrix}, \quad (\text{B14})$$

while all other exchange matrices can be obtained by applying the transformation of the single tetrahedron group T_d . For the explicit form of these exchange matrices we refer the reader to Ref. [57]. The relationship between the local and the global basis is given by the transformation

$$J_1 = \frac{1}{3} \left(-J_{zz} + 4J_{\pm} + 2J_{\pm\pm} + 2\sqrt{2}J_{z\pm} \right), \quad (\text{B15})$$

$$J_2 = \frac{1}{3} \left(J_{zz} - 4J_{\pm} + 4J_{\pm\pm} + 4\sqrt{2}J_{z\pm} \right), \quad (\text{B16})$$

$$J_3 = \frac{1}{3} \left(-J_{zz} - 2J_{\pm} - 4J_{\pm\pm} + 2\sqrt{2}J_{z\pm} \right), \quad (\text{B17})$$

$$J_4 = \frac{1}{3} \left(-J_{zz} - 2J_{\pm} + 2J_{\pm\pm} - \sqrt{2}J_{z\pm} \right). \quad (\text{B18})$$

In the global basis, the parametrization of the CSL 8 and 9 is given by $\{J_1, J_2, J_3, J_4\} = \left\{\frac{3J_{z\pm}}{\sqrt{2}}, \frac{3J_{z\pm}}{\sqrt{2}}, 0, 0\right\}$ and $\{J_1, J_2, J_3, J_4\} = \left\{-\frac{J_{z\pm}}{3\sqrt{2}}, \frac{7J_{z\pm}}{3\sqrt{2}}, \frac{4\sqrt{2}J_{z\pm}}{3}, -\frac{2\sqrt{2}J_{z\pm}}{3}\right\}$, respectively.

Appendix C: Irreducible representations and their exchange coefficients in the global basis

In the main text, we discussed the degeneracy of different magnetic orders using the irrep description with the spin degrees of freedom expressed in the local basis. In this appendix, we provide the irrep modes $\{\mathbf{m}_X\}$ in the global Cartesian basis as well as their exchange coefficients, a_X , in the global and in SVI basis above. Table IV gives the irrep modes in terms of the spin DOFs defined in the global basis while Table V gives the exchange coefficients, a_X , in terms of the global and SVI basis.

Appendix D: Correlation functions

In this appendix, we provide the expressions for the correlation functions presented in the main text. In reciprocal space, and for a generic non-Bravais lattice with a sublattice structure, the general correlation between spins is given by the expression

$$S_{\mu\nu}^{\alpha\gamma} = \langle S_{\mu}^{\alpha}(\mathbf{q}) S_{\nu}^{\gamma}(-\mathbf{q}) \rangle, \quad (\text{D1})$$

where μ, ν label the sublattices and α, β label the spin components. In particular, we compute the additive contribution of the spin-component diagonal elements of the general correlation function

$$\begin{aligned} \mathcal{S}(\mathbf{q}) &= \sum_{\alpha} \sum_{\mu, \nu} S_{\mu\nu}^{\alpha\alpha} \\ &= \sum_{\alpha} \sum_{\mu, \nu} \langle S_{\mu}^{\alpha}(\mathbf{q}) S_{\nu}^{\alpha}(-\mathbf{q}) \rangle, \end{aligned} \quad (\text{D2})$$

which, for short, we refer simply to as the spin structure factor. In addition to the spin structure factor, we have also computed the experimentally measurable unpolarized neutron structure factor, given by the expression

$$S_{\perp}(\mathbf{q}) = \sum_{\alpha, \beta} \sum_{\mu, \nu} (\delta_{\alpha, \beta} - \hat{\mathbf{q}}^{\alpha} \hat{\mathbf{q}}^{\beta}) \langle m_{\mu}^{\alpha}(\mathbf{q}) m_{\nu}^{\beta}(-\mathbf{q}) \rangle, \quad (\text{D3})$$

which measures the correlation between the magnetic moments, $\mathbf{m}_{i\mu}$, of the systems considered where the sub-index i labels the primitive FCC vectors \mathbf{R}_i and μ denotes the sublattice sites. The relationship between the magnetic moments and the spin degrees of freedom is provided by an anisotropic g -tensor

$$m_{i\mu}^{\alpha} = \sum_{\beta} g_{\mu}^{\alpha\beta} S_{i\mu}^{\beta}, \quad (\text{D4})$$

where $g_{\mu}^{\alpha\beta}$ are the components of the g -tensor associated to the μ -sublattice.

In addition to the unpolarized neutron structure factor, we have also considered the polarized neutron structure factor defined in terms of the incident neutrons' polarization \hat{z}_N [112]. This polarization analysis separates the neutron structure factor in Eq. (D3) into two channels, the non-spin-flip (NSF) channel which studies the correlations that are parallel to the incident polarization \hat{z}_N

$$S_{\perp}^{\text{NSF}}(\mathbf{q}) = \sum_{\alpha, \beta} \sum_{\mu, \nu} \left(\hat{z}_N^{\alpha} \hat{z}_N^{\beta} \right) \langle m_{\mu}^{\alpha} m_{\nu}^{\beta} \rangle, \quad (\text{D5})$$

and the spin-flip channel which is the complement of the NSF channel, defined as

$$S_{\perp}^{\text{SF}}(\mathbf{q}) = S_{\perp}(\mathbf{q}) - S_{\perp}^{\text{NSF}}(\mathbf{q}). \quad (\text{D6})$$

We note that the introduction of an anisotropic g -tensor in Eqs. (D3)-(D5) effectively ‘‘distorts’’ in momentum (\mathbf{q}) space the correlation functions we have presented [66, 103, 104] which were considered to discernibly expose the underlying gauge theory. For this reason, when reporting in the main text neutron structure factors (e.g. see Fig. 6), we chose an isotropic g -tensor (i.e. $g_{\mu}^{\alpha\beta} = g\delta_{\alpha\beta}$). To reiterate, in doing so, we make no assumptions on the nature (Kramers or non-Kramers) of the spin degrees of freedom in order to more clearly expose the underlying gauge theory of the CSLs considered.

Appendix E: Large- \mathcal{N}

The large- \mathcal{N} approximation, also known as the self-consistent Gaussian approximation (SCGA), is a classical approximation where the hard spin length constraint on the spin $|\mathbf{S}_i|^2 = S^2$ is replaced by a soft spin length constraint $\langle |\mathbf{S}_i|^2 \rangle = S^2$ which is energetically imposed by means of an introduced Lagrange multiplier λ . This approximation results in a Gaussian theory which can be exactly solved [113–116]. In this appendix we provide a minimal introduction to this approximation.

We first consider the generic bilinear Hamiltonian in Eq. (1), which can be written as

$$\mathcal{H} = \frac{1}{2} \sum_{i\mu, j\nu} \sum_{\alpha, \gamma} S_{i\mu}^{\alpha} J_{i\mu, j\nu}^{\alpha, \gamma} S_{j\nu}^{\gamma}, \quad (\text{E1})$$

where the sub-indices i and j label the primitive FCC vectors \mathbf{R}_i and μ and ν denote the sublattice basis. The generic spin-spin correlation function in \mathbf{q} space is given by

$$S_{\mu\nu}^{\alpha\gamma} = \langle S_{\mu}^{\alpha}(\mathbf{q}) S_{\nu}^{\gamma}(-\mathbf{q}) \rangle = \sum_{\mathbf{q}} (\beta \mathbf{J}_{\mu\nu}^{\alpha\gamma}(\mathbf{q}) + \lambda)^{-1}, \quad (\text{E2})$$

where the Lagrange multiplier λ is determined self consistently at every temperature $T = 1/\beta$ by solving the

TABLE IV. Relation between irreducible representations of the point group and the spins in the global basis.

Local order parameter field	Definition in terms of spin components
m_{A_2}	$\frac{1}{\sqrt{3}}(S_0^x + S_0^y + S_0^z + S_1^x - S_1^y - S_1^z - S_2^x + S_2^y - S_2^z - S_3^x - S_3^y + S_3^z)$
\mathbf{m}_E	$\begin{pmatrix} \frac{1}{\sqrt{6}}(-2S_0^x + S_0^y + S_0^z - 2S_1^x - S_1^y - S_1^z + 2S_2^x + S_2^y - S_2^z + 2S_3^x - S_3^y + S_3^z) \\ \frac{1}{\sqrt{2}}(-S_0^y + S_0^z + S_1^y - S_1^z - S_2^y - S_2^z + S_3^y + S_3^z) \end{pmatrix}$
\mathbf{m}_{T_2}	$\begin{pmatrix} \frac{1}{\sqrt{2}}(-S_0^y + S_0^z + S_1^y - S_1^z + S_2^y + S_2^z - S_3^y - S_3^z) \\ \frac{1}{\sqrt{2}}(S_0^x - S_0^z - S_1^x - S_1^z - S_2^x + S_2^z + S_3^x + S_3^z) \\ \frac{1}{\sqrt{2}}(-S_0^x + S_0^y + S_1^x + S_1^y - S_2^x - S_2^y + S_3^x - S_3^y) \end{pmatrix}$
$\mathbf{m}_{T_{1,i}}$	$\begin{pmatrix} \frac{1}{\sqrt{3}}(S_0^x + S_0^y + S_0^z + S_1^x - S_1^y - S_1^z + S_2^x - S_2^y + S_2^z + S_3^x + S_3^y - S_3^z) \\ \frac{1}{\sqrt{3}}(S_0^x + S_0^y + S_0^z - S_1^x + S_1^y + S_1^z - S_2^x + S_2^y - S_2^z + S_3^x + S_3^y - S_3^z) \\ \frac{1}{\sqrt{3}}(S_0^x + S_0^y + S_0^z - S_1^x + S_1^y + S_1^z + S_2^x - S_2^y + S_2^z - S_3^x - S_3^y + S_3^z) \end{pmatrix}$
$\mathbf{m}_{T_{1,p}}$	$\begin{pmatrix} \frac{1}{\sqrt{6}}(-2S_0^x + S_0^y + S_0^z - 2S_1^x - S_1^y - S_1^z - 2S_2^x - S_2^y + S_2^z - 2S_3^x + S_3^y - S_3^z) \\ \frac{1}{\sqrt{6}}(S_0^x - 2S_0^y + S_0^z - S_1^x - 2S_1^y + S_1^z - S_2^x - 2S_2^y - S_2^z + S_3^x - 2S_3^y - S_3^z) \\ \frac{1}{\sqrt{6}}(S_0^x + S_0^y - 2S_0^z - S_1^x + S_1^y - 2S_1^z + S_2^x - S_2^y - 2S_2^z - S_3^x - S_3^y - 2S_3^z) \end{pmatrix}$

TABLE V. Coefficients of the irreducible representations used in Eq. (3) and Eq. (B1)

Coefficient	Definition in terms of exchange parameters $\{J_1, J_2, J_3, J_4, D\}$	Definition in terms of exchange parameters $\{J, J_{\text{Ising}}, J_{\text{PD}}, J_{\text{DM}}, D\}$
a_{A_2}	$-2J_1 + J_2 - 2(J_3 + 2J_4) + D$	$-J - 4J_{\text{DM}} + 3J_{\text{Ising}} + D$
a_E	$-2J_1 + J_2 + J_3 + 2J_4$	$\frac{1}{2}(-2J + 4J_{\text{DM}} - J_{\text{PD}})$
a_{T_2}	$-J_2 + J_3 - 2J_4$	$\frac{1}{2}(-2J - 4J_{\text{DM}} + J_{\text{PD}})$
$a_{T_1 \text{ ice}}$	$\frac{1}{3}(2J_1 - J_2 + 2J_3 + 4J_4) + D$	$\frac{1}{3}(J + 4J_{\text{DM}} - 3J_{\text{Ising}} + 2J_{\text{PD}}) + D$
$a_{T_1 \text{ planar}}$	$\frac{1}{3}(4J_1 + J_2 - 5J_3 + 2J_4)$	$\frac{1}{6}(10J + 4J_{\text{DM}} - J_{\text{PD}})$
$a_{T_1 \text{ mixing}}$	$-\frac{4\sqrt{2}}{3}(J_1 + J_2 + J_3 - J_4)$	$-\frac{4\sqrt{2}}{3}(2J - J_{\text{DM}} + J_{\text{PD}})$

equation

$$S^2 = \frac{1}{N} \sum_{m, \mathbf{q}} (\beta \varepsilon_m(\mathbf{q}) + \lambda)^{-1}, \quad (\text{E3})$$

where $\varepsilon_m(\mathbf{q})$ corresponds to the m -th eigenvalue of the interaction matrix $\mathbf{J}_{i\mu, j\nu}^{\alpha, \gamma}$ expressed in momentum space, $\mathbf{J}_{\mu\nu}^{\alpha, \gamma}(\mathbf{q})$.

-
- [1] X.-G. Wen, *Quantum Field Theory of Many-Body Systems* (Oxford University Press, 2007).
- [2] L. Balents, Spin liquids in frustrated magnets, *Nature* **464**, 199 (2010).
- [3] C. Lacroix, P. Mendels, and F. Mila, *Introduction to Frustrated Magnetism* (Springer, 2011).
- [4] Y. Zhou, K. Kanoda, and T.-K. Ng, Quantum spin liquid states, *Rev. Mod. Phys.* **89**, 025003 (2017).
- [5] L. Savary and L. Balents, Quantum spin liquids: A review, *Rep. Prog. Phys.* **80**, 016502 (2016).
- [6] M. J. P. Gingras and P. A. McClarty, Quantum spin ice: a search for gapless quantum spin liquids in pyrochlore magnets, *Reports on Progress in Physics* **77**, 056501 (2014).
- [7] J. Knolle and R. Moessner, A field guide to spin liquids, *Annu. Rev. Condens. Matter Phys.* **10**, 451 (2019).
- [8] R. Moessner and J. E. Moore, *Topological Phases of Matter* (Cambridge University Press, 2021).
- [9] H. Yan, O. Benton, R. Moessner, and A. H. Nevidomskyy, Classification of classical spin liquids: Typology and resulting landscape, *Phys. Rev. B* **110**, L020402 (2024).
- [10] H. Yan, O. Benton, A. H. Nevidomskyy, and R. Moessner, Classification of classical spin liquids: Detailed formalism and suite of examples, *Phys. Rev. B* **109**, 174421 (2024).

- [11] Y. Fang, J. Cano, A. H. Nevidomskyy, and H. Yan, Classification of classical spin liquids: Topological quantum chemistry and crystalline symmetry, *Phys. Rev. B* **110**, 054421 (2024).
- [12] D. L. Bergman, C. Wu, and L. Balents, Band touching from real-space topology in frustrated hopping models, *Phys. Rev. B* **78**, 125104 (2008).
- [13] J. Villain, Insulating spin glasses, *Zeitschrift für Physik B - Condensed Matter* **33**, 31 (1979).
- [14] J. S. Gardner, M. J. P. Gingras, and J. E. Greedan, Magnetic pyrochlore oxides, *Rev. Mod. Phys.* **82**, 53 (2010).
- [15] A. M. Hallas, J. Gaudet, and B. D. Gaulin, Experimental insights into ground-state selection of quantum xy pyrochlores, *Annu. Rev. Condens. Matter Phys.* **9**, 105 (2018).
- [16] J. G. Rau and M. J. P. Gingras, Frustrated quantum rare-earth pyrochlores, *Annual Review of Condensed Matter Physics* **10**, 357 (2019).
- [17] E. M. Smith, E. Lhotel, S. Petit, and B. D. Gaulin, *Annual Review of Condensed Matter Physics* **16**, 387 (2025).
- [18] M. J. Harris, S. T. Bramwell, D. F. McMorrow, T. Zeiske, and K. W. Godfrey, Geometrical frustration in the ferromagnetic pyrochlore $\text{Ho}_2\text{Ti}_2\text{O}_7$, *Phys. Rev. Lett.* **79**, 2554 (1997).
- [19] S. T. Bramwell and M. J. P. Gingras, Spin ice state in frustrated magnetic pyrochlore materials, *Science* **294**, 1495 (2001).
- [20] C. Castelnovo, R. Moessner, and S. Sondhi, Spin Ice, Fractionalization, and Topological Order, *Annual Review of Condensed Matter Physics* **3**, 35 (2012).
- [21] M. Udagawa and L. Jaubert, eds., *Spin Ice*, Springer Series in Solid-State Sciences, Vol. 197 (Springer International Publishing, Cham, 2021).
- [22] S. T. Bramwell, M. J. Harris, B. C. den Hertog, M. J. P. Gingras, J. S. Gardner, D. F. McMorrow, A. R. Wildes, A. L. Cornelius, J. D. M. Champion, R. G. Melko, and T. Fennell, Spin correlations in $\text{Ho}_2\text{Ti}_2\text{O}_7$: A dipolar spin ice system, *Phys. Rev. Lett.* **87**, 047205 (2001).
- [23] T. Fennell, O. A. Petrenko, B. Fåk, J. S. Gardner, S. T. Bramwell, and B. Ouladdiaf, Neutron scattering studies of the spin ices $\text{Ho}_2\text{Ti}_2\text{O}_7$ and $\text{Dy}_2\text{Ti}_2\text{O}_7$ in applied magnetic field, *Phys. Rev. B* **72**, 224411 (2005).
- [24] T. Fennell, P. P. Deen, A. R. Wildes, K. Schmalzl, D. Prabhakaran, A. T. Boothroyd, R. J. Aldus, D. F. McMorrow, and S. T. Bramwell, Magnetic Coulomb phase in the Spin Ice $\text{Ho}_2\text{Ti}_2\text{O}_7$, *Science* **326**, 415 (2009).
- [25] A. P. Ramirez, A. Hayashi, R. J. Cava, R. Siddharthan, and B. S. Shastry, Zero-point entropy in 'spin ice', *Nature* **399**, 333 (1999).
- [26] T. Fennell, O. A. Petrenko, B. Fåk, S. T. Bramwell, M. Enjalran, T. Yavors'kii, M. J. P. Gingras, R. G. Melko, and G. Balakrishnan, Neutron scattering investigation of the spin ice state in $\text{Dy}_2\text{Ti}_2\text{O}_7$, *Phys. Rev. B* **70**, 134408 (2004).
- [27] D. J. P. Morris, D. A. Tennant, S. A. Grigera, B. Klemke, C. Castelnovo, R. Moessner, C. Czternasty, M. Meissner, K. C. Rule, J.-U. Hoffmann, K. Kiefer, S. Gerischer, D. Slobinsky, and R. S. Perry, Dirac strings and magnetic monopoles in the spin ice $\text{Dy}_2\text{Ti}_2\text{O}_7$, *Science* **326**, 411 (2009).
- [28] C. L. Henley, The "Coulomb phase" in frustrated systems, *Annual Review of Condensed Matter Physics* **1**, 179 (2010).
- [29] C. Castelnovo, R. Moessner, and S. L. Sondhi, Magnetic monopoles in spin ice, *Nature* **451**, 42 (2008).
- [30] J. G. Rau and M. J. P. Gingras, Magnitude of quantum effects in classical spin ices, *Phys. Rev. B* **92**, 144417 (2015).
- [31] H. D. Zhou, J. G. Cheng, A. M. Hallas, C. R. Wiebe, G. Li, L. Balicas, J. S. Zhou, J. B. Goodenough, J. S. Gardner, and E. S. Choi, Chemical pressure effects on pyrochlore spin ice, *Phys. Rev. Lett.* **108**, 207206 (2012).
- [32] M. Hermele, M. P. A. Fisher, and L. Balents, Pyrochlore photons: The $u(1)$ spin liquid in a $s = \frac{1}{2}$ three-dimensional frustrated magnet, *Phys. Rev. B* **69**, 064404 (2004).
- [33] H. R. Molavian, M. J. P. Gingras, and B. Canals, Dynamically induced frustration as a route to a quantum spin ice state in $\text{Tb}_2\text{Ti}_2\text{O}_7$ via virtual crystal field excitations and quantum many-body effects, *Phys. Rev. Lett.* **98**, 157204 (2007).
- [34] S. Onoda and Y. Tanaka, Quantum melting of spin ice: Emergent cooperative quadrupole and chirality, *Phys. Rev. Lett.* **105**, 047201 (2010).
- [35] S. Lee, S. Onoda, and L. Balents, Generic quantum spin ice, *Phys. Rev. B* **86**, 104412 (2012).
- [36] O. Benton, O. Sikora, and N. Shannon, Seeing the light: Experimental signatures of emergent electromagnetism in a quantum spin ice, *Phys. Rev. B* **86**, 075154 (2012).
- [37] N. Shannon, O. Sikora, F. Pollmann, K. Penc, and P. Fulde, Quantum Ice: A Quantum Monte Carlo Study, *Physical Review Letters* **108**, 067204 (2012).
- [38] C.-J. Huang, Y. Deng, Y. Wan, and Z. Y. Meng, Dynamics of topological excitations in a model quantum spin ice, *Phys. Rev. Lett.* **120**, 167202 (2018).
- [39] O. Benton, Ground-state phase diagram of dipolar-octupolar pyrochlores, *Phys. Rev. B* **102**, 104408 (2020).
- [40] S. D. Pace, S. C. Morampudi, R. Moessner, and C. R. Laumann, Emergent fine structure constant of quantum spin ice is large, *Phys. Rev. Lett.* **127**, 117205 (2021).
- [41] M. Hosoi, E. Z. Zhang, A. S. Patri, and Y. B. Kim, Uncovering Footprints of Dipolar-Octupolar Quantum Spin Ice from Neutron Scattering Signatures, *Physical Review Letters* **129**, 097202 (2022).
- [42] F. Desrochers and Y. B. Kim, Spectroscopic signatures of fractionalization in octupolar quantum spin ice, *Phys. Rev. Lett.* **132**, 066502 (2024).
- [43] H. Yan, A. Sanders, C. Castelnovo, and A. H. Nevidomskyy, Experimentally tunable qed in dipolar-octupolar quantum spin ice, arXiv:2312.11641 10.48550/arXiv.2312.11641 (2023).
- [44] K. Kimura, S. Nakatsuji, J.-J. Wen, C. Broholm, M. B. Stone, E. Nishibori, and H. Sawa, Quantum fluctuations in spin-ice-like $\text{Pr}_2\text{Zr}_2\text{O}_7$, *Nature Communications* **4**, 1934 (2013).
- [45] N. Martin, P. Bonville, E. Lhotel, S. Guitteny, A. Wildes, C. Decorse, M. Ciomaga Hatnean, G. Balakrishnan, I. Mirebeau, and S. Petit, Disorder and quantum spin ice, *Phys. Rev. X* **7**, 041028 (2017).
- [46] R. Sibille, N. Gauthier, H. Yan, M. Ciomaga Hatnean, J. Ollivier, B. Winn, U. Filges, G. Balakrishnan, M. Kenzelmann, N. Shannon, and T. Fennell, Experi-

- mental signatures of emergent quantum electrodynamics in $\text{Pr}_2\text{Hf}_2\text{O}_7$, *Nature Physics* **14**, 711 (2018).
- [47] B. Gao, T. Chen, D. W. Tam, C.-L. Huang, K. Sasmal, D. T. Adroja, F. Ye, H. Cao, G. Sala, M. B. Stone, C. Baines, J. A. T. Verezhak, H. Hu, J.-H. Chung, X. Xu, S.-W. Cheong, M. Nallaiyan, S. Spagna, M. B. Maple, A. H. Nevidomskyy, E. Morosan, G. Chen, and P. Dai, Experimental signatures of a three-dimensional quantum spin liquid in effective spin-1/2 $\text{Ce}_2\text{Zr}_2\text{O}_7$ pyrochlore, *Nature Physics* **15**, 1052 (2019).
- [48] J. Gaudet, E. M. Smith, J. Dudemaine, J. Beare, C. R. C. Buhariwalla, N. P. Butch, M. B. Stone, A. I. Kolesnikov, G. Xu, D. R. Yahne, K. A. Ross, C. A. Marjerrison, J. D. Garrett, G. M. Luke, A. D. Bianchi, and B. D. Gaulin, Quantum spin ice dynamics in the dipole-octupole pyrochlore magnet $\text{Ce}_2\text{Zr}_2\text{O}_7$, *Phys. Rev. Lett.* **122**, 187201 (2019).
- [49] R. Sibille, N. Gauthier, E. Lhotel, V. Porée, V. Pomjakushin, R. A. Ewings, T. G. Perring, J. Ollivier, A. Wildes, C. Ritter, T. C. Hansen, D. A. Keen, G. J. Nilsen, L. Keller, S. Petit, and T. Fennell, A quantum liquid of magnetic octupoles on the pyrochlore lattice, *Nature Physics* **16**, 546 (2020).
- [50] V. Porée, H. Yan, F. Desrochers, S. Petit, E. Lhotel, M. Appel, J. Ollivier, Y. B. Kim, A. H. Nevidomskyy, and R. Sibille, Fractional matter coupled to the emergent gauge field in a quantum spin ice (2023), [arXiv:2304.05452](https://arxiv.org/abs/2304.05452).
- [51] B. Gao, F. Desrochers, D. W. Tam, P. Steffens, A. Hiess, Y. Su, S.-W. Cheong, Y. B. Kim, and P. Dai, Emergent photons and fractionalized excitations in a quantum spin liquid (2024), [arXiv:2404.04207](https://arxiv.org/abs/2404.04207) [cond-mat.str-el].
- [52] E. M. Smith, J. Dudemaine, B. Placke, R. Schäfer, D. R. Yahne, T. DeLazzer, A. Fitterman, J. Beare, J. Gaudet, C. R. C. Buhariwalla, A. Podlesnyak, G. Xu, J. P. Clancy, R. Movshovich, G. M. Luke, K. A. Ross, R. Moessner, O. Benton, A. D. Bianchi, and B. D. Gaulin, Quantum spin ice response to a magnetic field in the dipole-octupole pyrochlore $\text{Ce}_2\text{Zr}_2\text{O}_7$, *Phys. Rev. B* **108**, 054438 (2023).
- [53] D. R. Yahne, B. Placke, R. Schäfer, O. Benton, R. Moessner, M. Powell, J. W. Kolis, C. M. Pasco, A. F. May, M. D. Frontzek, E. M. Smith, B. D. Gaulin, S. Calder, and K. A. Ross, Dipolar spin ice regime proximate to an all-in-all-out néel ground state in the dipolar-octupolar pyrochlore $\text{Ce}_2\text{Sn}_2\text{O}_7$, *Phys. Rev. X* **14**, 011005 (2024).
- [54] S. H. Curnoe, Structural distortion and the spin liquid state in $\text{Tb}_2\text{Ti}_2\text{O}_7$, *Phys. Rev. B* **78**, 094418 (2008).
- [55] J. D. Thompson, P. A. McClarty, H. M. Rønnow, L. P. Regnault, A. Sørge, and M. J. P. Gingras, Rods of neutron scattering intensity in $\text{Yb}_2\text{Ti}_2\text{O}_7$: Compelling evidence for significant anisotropic exchange in a magnetic pyrochlore oxide, *Phys. Rev. Lett.* **106**, 187202 (2011).
- [56] K. A. Ross, L. Savary, B. D. Gaulin, and L. Balents, Quantum excitations in quantum spin ice, *Phys. Rev. X* **1**, 021002 (2011).
- [57] H. Yan, O. Benton, L. Jaubert, and N. Shannon, Theory of multiple-phase competition in pyrochlore magnets with anisotropic exchange with application to $\text{Yb}_2\text{Ti}_2\text{O}_7$, $\text{Er}_2\text{Ti}_2\text{O}_7$, and $\text{Er}_2\text{Sn}_2\text{O}_7$, *Phys. Rev. B* **95**, 094422 (2017).
- [58] K. T. K. Chung, Mapping the Phase Diagram of a Frustrated Magnet: Degeneracies, Flat Bands, and Canting Cycles on the Pyrochlore Lattice (2024), [arXiv:2411.03429](https://arxiv.org/abs/2411.03429) [cond-mat.str-el].
- [59] C. Xu, Gapless bosonic excitation without symmetry breaking: An algebraic spin liquid with soft gravitons, *Phys. Rev. B* **74**, 224433 (2006).
- [60] M. Pretko, Subdimensional particle structure of higher rank $u(1)$ spin liquids, *Phys. Rev. B* **95**, 115139 (2017).
- [61] M. Pretko, Generalized electromagnetism of subdimensional particles: A spin liquid story, *Phys. Rev. B* **96**, 035119 (2017).
- [62] J. N. Reimers, Absence of long-range order in a three-dimensional geometrically frustrated antiferromagnet, *Physical Review B* **45**, 7287 (1992).
- [63] R. Moessner and J. T. Chalker, Low-temperature properties of classical geometrically frustrated antiferromagnets, *Phys. Rev. B* **58**, 12049 (1998).
- [64] M. Taillefumier, O. Benton, H. Yan, L. D. C. Jaubert, and N. Shannon, Competing spin liquids and hidden spin-nematic order in spin ice with frustrated transverse exchange, *Phys. Rev. X* **7**, 041057 (2017).
- [65] O. Benton, L. Jaubert, H. Yan, and N. Shannon, A spin-liquid with pinch-line singularities on the pyrochlore lattice, *Nature Communications* **7**, 10.1038/ncomms11572 (2016).
- [66] D. Lozano-Gómez, V. Noculak, J. Oitmaa, R. R. P. Singh, Y. Iqbal, J. Reuther, and M. J. P. Gingras, Competing gauge fields and entropically driven spin liquid to spin liquid transition in non-Kramers pyrochlores, *Proceedings of the National Academy of Sciences* **121**, e2403487121 (2024).
- [67] M. Pretko, X. Chen, and Y. You, Fracton phases of matter, *International Journal of Modern Physics A* **35**, 2030003 (2020).
- [68] R. M. Nandkishore and M. Hermele, Fractons, *Annual Review of Condensed Matter Physics* **10**, 295 (2019).
- [69] Y. You, Quantum liquids: Emergent higher-rank gauge theory and fractons (2024), [arXiv:2403.17074](https://arxiv.org/abs/2403.17074) [cond-mat.str-el].
- [70] S. Vijay, J. Haah, and L. Fu, A new kind of topological quantum order: A dimensional hierarchy of quasiparticles built from stationary excitations, *Phys. Rev. B* **92**, 235136 (2015).
- [71] C. Chamon, Quantum glassiness in strongly correlated clean systems: An example of topological overprotection, *Phys. Rev. Lett.* **94**, 040402 (2005).
- [72] J. Haah, Local stabilizer codes in three dimensions without string logical operators, *Phys. Rev. A* **83**, 042330 (2011).
- [73] L. Savary, X. Wang, H.-Y. Kee, Y. B. Kim, Y. Yu, and G. Chen, Quantum spin ice on the breathing pyrochlore lattice, *Phys. Rev. B* **94**, 075146 (2016).
- [74] H. Yan, O. Benton, L. D. C. Jaubert, and N. Shannon, Rank-2 $U(1)$ Spin Liquid on the Breathing Pyrochlore Lattice, *Phys. Rev. Lett.* **124**, 127203 (2020).
- [75] A. W. C. Wong, Z. Hao, and M. J. P. Gingras, Ground state phase diagram of generic xy pyrochlore magnets with quantum fluctuations, *Phys. Rev. B* **88**, 144402 (2013).
- [76] L. Savary, K. A. Ross, B. D. Gaulin, J. P. C. Ruff, and L. Balents, Order by quantum disorder in $\text{Er}_2\text{Ti}_2\text{O}_7$, *Phys. Rev. Lett.* **109**, 167201 (2012).
- [77] S. Guitteny, S. Petit, E. Lhotel, J. Robert, P. Bonville, A. Forget, and I. Mirebeau, Palmer-chalker correlations

- in the xy pyrochlore antiferromagnet $\text{Er}_2\text{Sn}_2\text{O}_7$, *Phys. Rev. B* **88**, 134408 (2013).
- [78] L. D. C. Jaubert, O. Benton, J. G. Rau, J. Oitmaa, R. R. P. Singh, N. Shannon, and M. J. P. Gingras, Are multiphase competition and order by disorder the keys to understanding $\text{Yb}_2\text{Ti}_2\text{O}_7$, *Phys. Rev. Lett.* **115**, 267208 (2015).
- [79] C. L. Sarkis, J. G. Rau, L. D. Sanjeeva, M. Powell, J. Kolis, J. Marbey, S. Hill, J. A. Rodriguez-Rivera, H. S. Nair, D. R. Yahne, S. Säubert, M. J. P. Gingras, and K. A. Ross, Unravelling competing microscopic interactions at a phase boundary: A single-crystal study of the metastable antiferromagnetic pyrochlore $\text{Yb}_2\text{Ge}_2\text{O}_7$, *Phys. Rev. B* **102**, 134418 (2020).
- [80] A. Scheie, J. Kindervater, S. Zhang, H. J. Changlani, G. Sala, G. Ehlers, A. Heinemann, G. S. Tucker, S. M. Koohpayeh, and C. Broholm, Multiphase magnetism in $\text{Yb}_2\text{Ti}_2\text{O}_7$, *Proceedings of the National Academy of Sciences* **117**, 27245 (2020).
- [81] E. M. Smith, J. Dudemaine, B. Placke, R. Schäfer, D. R. Yahne, T. DeLazzer, A. Fitterman, J. Beare, J. Gaudet, C. R. C. Buhariwalla, A. Podlesnyak, G. Xu, J. P. Clancy, R. Movshovich, G. M. Luke, K. A. Ross, R. Moessner, O. Benton, A. D. Bianchi, and B. D. Gaulin, Quantum spin ice response to a magnetic field in the dipole-octupole pyrochlore $\text{Ce}_2\text{Zr}_2\text{O}_7$, *Phys. Rev. B* **108**, 054438 (2023).
- [82] R. Moessner and J. T. Chalker, Properties of a classical spin liquid: The Heisenberg pyrochlore antiferromagnet, *Phys. Rev. Lett.* **80**, 2929 (1998).
- [83] A. Bertin, Y. Chapuis, P. D. de Réotier, and A. Yaouanc, Crystal electric field in the $\text{R}_2\text{Ti}_2\text{O}_7$ pyrochlore compounds, *Journal of Physics: Condensed Matter* **24**, 256003 (2012).
- [84] J. Gaudet, A. M. Hallas, A. I. Kolesnikov, and B. D. Gaulin, Effect of chemical pressure on the crystal electric field states of erbium pyrochlore magnets, *Physical Review B* **97**, 024415 (2017).
- [85] A. Roll, V. Balédent, J. Robert, J. Ollivier, C. Decorse, S. Guitteny, I. Mirebeau, and S. Petit, Magnetic interactions in the cooperative paramagnet $\text{Tb}_2\text{Ti}_2\text{O}_7$, *Phys. Rev. Res.* **6**, 043011 (2024).
- [86] P. A. McClarty, S. H. Curnoe, and M. J. P. Gingras, Energetic selection of ordered states in a model of the $\text{Er}_2\text{Ti}_2\text{O}_7$ frustrated pyrochlore xy antiferromagnet, *Journal of Physics: Conference Series* **145**, 012032 (2009).
- [87] S. Petit, J. Robert, S. Guitteny, P. Bonville, C. Decorse, J. Ollivier, H. Mutka, M. J. P. Gingras, and I. Mirebeau, Order by disorder or energetic selection of the ground state in the xy pyrochlore antiferromagnet $\text{Er}_2\text{Ti}_2\text{O}_7$: An inelastic neutron scattering study, *Phys. Rev. B* **90**, 060410 (2014).
- [88] J. G. Rau, S. Petit, and M. J. P. Gingras, Order by virtual crystal field fluctuations in pyrochlore xy antiferromagnets, *Phys. Rev. B* **93**, 184408 (2016).
- [89] S. Onoda and Y. Tanaka, Quantum fluctuations in the effective pseudospin- $\frac{1}{2}$ model for magnetic pyrochlore oxides, *Phys. Rev. B* **83**, 094411 (2011).
- [90] Y.-P. Huang, G. Chen, and M. Hermele, Quantum spin ices and topological phases from dipolar-octupolar doublets on the pyrochlore lattice, *Phys. Rev. Lett.* **112**, 167203 (2014).
- [91] N. Iwahara and L. F. Chibotaru, Exchange interaction between J multiplets, *Phys. Rev. B* **91**, 174438 (2015).
- [92] A. Sadeghi, M. Alaei, F. Shahbazi, and M. J. P. Gingras, Spin Hamiltonian, order out of a Coulomb phase, and pseudocriticality in the frustrated pyrochlore Heisenberg antiferromagnet FeF_3 , *Phys. Rev. B* **91**, 140407 (2015).
- [93] S. Zhang, H. J. Changlani, K. W. Plumb, O. Tchernyshyov, and R. Moessner, Dynamical structure factor of the three-dimensional quantum spin liquid candidate $\text{NaCaNi}_2\text{F}_7$, *Phys. Rev. Lett.* **122**, 167203 (2019).
- [94] N. Francini, L. Janssen, and D. Lozano-Gómez, Higher-rank spin liquids and spin nematics from competing orders in pyrochlore magnets, *Phys. Rev. B* **111**, 085140 (2025).
- [95] J. Villain, R. Bidaux, J.-P. Carton, and R. Conte, Order as an effect of disorder, *J. Phys. France*, **41**, 1263 (1980).
- [96] M. E. Zhitomirsky, M. V. Gvozdikova, P. C. W. Holdsworth, and R. Moessner, Quantum Order by Disorder and Accidental Soft Mode in $\text{Er}_2\text{Ti}_2\text{O}_7$, *Phys. Rev. Lett.* **109**, 077204 (2012).
- [97] M. Pretko, Subdimensional particle structure of higher rank $U(1)$ spin liquids, *Phys. Rev. B* **95**, 115139 (2017).
- [98] M. Pretko, The fracton gauge principle, *Phys. Rev. B* **98**, 115134 (2018).
- [99] Y. Katayama, T. Mizutani, W. Utsumi, O. Shimomura, M. Yamakata, and K. Funakoshi, A first-order liquid-liquid phase transition in phosphorus, *Nature (London)* **403**, 170 (2000).
- [100] L. Henry, M. Mezouar, G. Garbarino, D. Sifré, G. Weck, and F. Datchi, Liquid-liquid transition and critical point in sulfur, *Nature (London)* **584**, 382 (2020).
- [101] M. Beye, F. Sorgenfrei, W. F. Schlotter, W. Wurth, and A. Fohlisch, The liquid-liquid phase transition in silicon revealed by snapshots of valence electrons, *Proc. Natl. Acad. Sci. U.S.A.* **107**, 16772 (2010).
- [102] H. Takatsu, S. Onoda, S. Kittaka, A. Kasahara, Y. Kono, T. Sakakibara, Y. Kato, B. Fåk, J. Ollivier, J. W. Lynn, T. Taniguchi, M. Wakita, and H. Kadowaki, Quadrupole order in the frustrated pyrochlore $\text{tb}_{2+x}\text{ti}_{2-x}\text{o}_{7+y}$, *Phys. Rev. Lett.* **116**, 217201 (2016).
- [103] H. Kadowaki, H. Takatsu, T. Taniguchi, B. Fåk, and J. Ollivier, Composite spin and quadrupole wave in the ordered phase of $\text{Tb}_{2+x}\text{Ti}_{2-x}\text{O}_{7+y}$, *SPIN* **05**, 1540003 (2015).
- [104] C. Castelnovo and R. Moessner, Rod motifs in neutron scattering in spin ice, *Phys. Rev. B* **99**, 121102 (2019).
- [105] J. D. Alzate-Cardona, D. Sabogal-Suárez, R. F. L. Evans, and E. Restrepo-Parra, Optimal phase space sampling for Monte Carlo simulations of Heisenberg spin systems, *J. Phys. Condens. Matter* **31**, 095802 (2019).
- [106] M. Creutz, Overrelaxation and Monte Carlo simulation, *Phys. Rev. D* **36**, 515 (1987).
- [107] J. G. Rau and M. J. P. Gingras, Spin slush in an extended spin ice model, *Nat. Comm.* **7**, 12234 (2016).
- [108] K. T. K. Chung and M. J. P. Gingras, 2-form $u(1)$ spin liquids: A classical model and quantum aspects, *Phys. Rev. B* **111**, 064417 (2025).
- [109] H. Yan, O. Benton, L. D. C. Jaubert, and N. Shannon, Rank-2 $u(1)$ spin liquid on the breathing pyrochlore lattice, *Phys. Rev. Lett.* **124**, 127203 (2020).
- [110] L. Gresista, D. Lozano-Gómez, M. Vojta, S. Trebst,

- and Y. Iqbal, Quantum effects on pyrochlore higher-rank U(1) spin liquids: pinch-line singularities, spin nematics, and connections to oxide materials (2025), [arXiv:2503.03749 \[cond-mat.str-el\]](https://arxiv.org/abs/2503.03749).
- [111] V. Noculak, D. Lozano-Gómez, J. Oitmaa, R. R. P. Singh, Y. Iqbal, M. J. P. Gingras, and J. Reuther, Classical and quantum phases of the pyrochlore $s = \frac{1}{2}$ magnet with Heisenberg and Dzyaloshinskii-Moriya interactions, *Phys. Rev. B* **107**, 214414 (2023).
- [112] K. T. K. Chung, J. S. K. Goh, A. Mukherjee, W. Jin, D. Lozano-Gómez, and M. J. P. Gingras, Probing flat band physics in spin ice systems via polarized neutron scattering, *Phys. Rev. Lett.* **128**, 107201 (2022).
- [113] P. H. Conlon and J. T. Chalker, Absent pinch points and emergent clusters: Further neighbor interactions in the pyrochlore Heisenberg antiferromagnet, *Phys. Rev. B* **81**, 224413 (2010).
- [114] D. A. Garanin and B. Canals, Classical spin liquid: Exact solution for the infinite-component antiferromagnetic model on the kagomé lattice, *Phys. Rev. B* **59**, 443 (1999).
- [115] B. Canals and D. A. Garanin, Classical spin liquid properties of the infinite-component spin vector model on a fully frustrated two dimensional lattice, *The European Physical Journal B - Condensed Matter and Complex Systems* **26**, 439 (2002).
- [116] B. Canals and D. A. Garanin, Spin-liquid phase in the pyrochlore anti-ferromagnet, *Canadian Journal of Physics* **79**, 1323 (2001), <https://doi.org/10.1139/p01-101>.